**FACULTY
OF MATHEMATICS
AND PHYSICS**
Charles University

MASTER THESIS

Miroslav Šlechta

Charge transport in halide perovskites affected by the surface treatment and metalization

Institute of Physics of Charles University

Supervisor of the master thesis: doc. Ing. Eduard Belas, CSc.

Study programme: Physics

Study branch: Optics and Optoelectronics

Prague 2023

I declare that I carried out this master thesis independently, and only with the cited sources, literature and other professional sources. It has not been used to obtain another or the same degree.

I understand that my work relates to the rights and obligations under the Act No. 121/2000 Sb., the Copyright Act, as amended, in particular the fact that the Charles University has the right to conclude a license agreement on the use of this work as a school work pursuant to Section 60 subsection 1 of the Copyright Act.

In .... date ....
                                                   Author's signature

Title: Charge transport in halide perovskites affected by the surface treatment and metalization

Author: Miroslav Šlechta

Institute: Institute of Physics of Charles University

Supervisor: doc. Ing. Eduard Belas, CSc., Institute of Physics of Charles University

Abstract: In this thesis, I study charge transport in halide perovskites. This is done using the characterization method, which here is the I-V characteristics. It studies the effect of current and voltage on the prepared sample, also at different temperatures. A significant sensitivity of the material to the measurement history was found. Derived evaluations of this measurement technique further provide possibilities for the detection of hysteresis behavior as well as the evaluation of measurements over time to determine the temporal stability of carrier collection. This also proved the phenomenon of electromigration of defects. Furthermore, transport parameters were calculated from the time measurements, which point to their non-monotonic development in increasing temperatures. A theoretical model explaining such behavior was proposed as a possibility for further research on perovskites and development of this topic.

Keywords: metal-semiconductor contact, halide perovskites, charge transport

Contents

1. Introduction

1.1 Motivation

Perovskites have gained, especially in the last two decades, considerable attention from a wide number of scientific groups around the world, for their excellent optoelectronic properties. These are primarily the existence of electrically inactive defects, high carrier mobility, its long diffusion length and a large absorption coefficient. Considering the mentioned properties, easy preparation and low cost of crystal production, perovskites have considerable application potential in the field of optoelectronic devices including photovoltaic cells, light-emitting diodes, lasers, photodetectors, X-ray and gamma radiation detectors, phototransistors and field-controlled transistors. The performance of optoelectronic devices based on organic-inorganic hybrid perovskites is so far limited, as the organic components can be easily decomposed by moisture, oxygen, heat and and radiation under ambient circumstance. Completely inorganic perovskites, which replace the organic group with inorganic components, have advanced stability in this direction. Single crystals, which retain the intrinsic properties of perovskites, have far fewer defects and grain boundaries, unlike polycrystalline layers, play a key role in basic materials research and the design of efficient optoelectronic devices. The $CsPbBr_3$ inorganic perovskite appears in particular as a representative. Another modification of this structure is the introduction of mixed metal perovskite compositions Pb/Sn, which allow to realize narrower bandgaps that cannot be achieved with a pure Pb variant. This has achieved significant results for multijunction perovskite photovoltaic cells and also for light-emitting diodes in the near-infrared region. Although their optoelectronic properties have already been intensively studied in the past, a detailed understanding of the physics of charge transport is still lacking.[1]

In this diploma thesis, I study charge transport in the perovskite structure $CsPbBr_3$ depending on the different conditions of sample preparation, in terms of their surface treatment and variants of the electrical contacts used. The fundamental technique used for this purpose is the measurement of current-voltage characteristics, including the evaluation of their hysteresis behavior, as well as the measurement of the dependence and development of the mentioned quantities in time and temperature. [18]

The essencial reason of my study and decision for it stays, that the subject matter of such transport is actual, fundamental for the performance, but itself was not fully explained yet. A number of groups is coming with various results and surveys, but clear answers heretofore no one set forth. Therefore, I would like to explore this issue in the direction, which was primarily given by three publications in spite of the fact that their conclusions remain still slightly opened. Initially *Xiao et al.*[2], who primarily observed current-voltage hysteresis behavior, resp. variety of hysteresis loops with changed scanning rates, whereas current density remains unchanged.

Next was *Eames et al.*[3] who concern of ionic transport and observed that ion migration is a factor contributing to unusual behaviour, including current–voltage hysteresis. Also reached of opinion that halide perovskites are mixed ionic-

electronic conductors. Subsequently *Zhao et al.*[4] study correlations between immobilizing ions and suppressing hysteresis in halide perovskites.

1.2   Perovskites

1.2.1   Origin

The research on perovskite materials dates back to 1839 when crystallographer Gustav Rose determined its composition. The perovskite mineral was discovered in the Ural Mountains of Russia by mineral collector August Kämmerer. It was a black mineral and its composition was calcium titanate $CaTiO_3$. Kämmerer requested that the new mineral be named in honor of mineralogist Lev Alekseyevich Perovski. Researches on these oxide perovskites have led to their industrial applications in electronic devices. The high dielectric constant discovered for $BaTiO_3$ has led the industry of ferroelectrics such as capacitors, superconductors, piezoelectric devices, proton conductors, fuel cells, and memory storage devices. Although other metal oxide perovskites, such as $BaTiO_3$, $LiNbO_3$, $PbTiO_3$, $SrTiO_3$ and $BiFeO_3$, also work as ferroelectric ceramics and some of them have been found to exhibit photovoltaic functions. [26], [27] However, these oxide perovskites have large bandgaps (more than 2.5 eV) that lack in light-harvesting ability and exhibit low efficiency in the collection of free charges. Therefore, oxide perovskites do not exhibit good semiconducting properties suitable for photovoltaic absorbers. [7], [19], [20], [21]

1.2.2   Halide Perovkites

Perovskite generally represents a type of crystal structure with the chemical formula ABX_3 , where A and B are alkali and metal cations, respectively, and X is an anion as shown in Figure *1.1*.[1] In an ideal cubic structure, the B cation
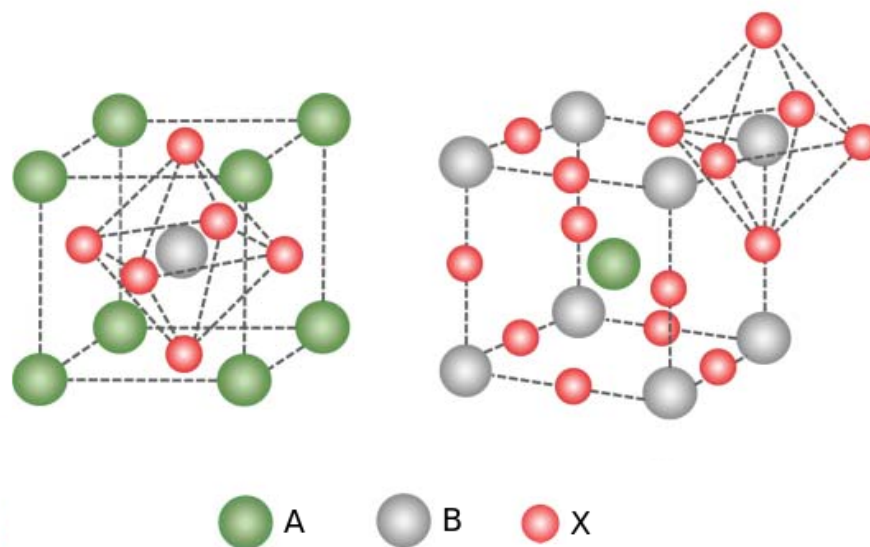

Figure 1.1: General crystal structure of perovskite, ABX_3 (X is oxygen or halogen)[7]

has a sixfold configuration, surrounded by an octahedron of anions, and the A cation is in a 12-fold cuboctahedral configuration with coordination of 12 anions as shown in Figure *1.1 right.* The cubic unit cell of such compounds consists of A cations at the cube corner positions, B sitting at the body-center position, and X anions occupying the face-centered positions. Before halide perovskites attracted attention as photovoltaic semiconductors, perovskites were generally known as inorganic metal oxides (A = alkali cation, X = oxygen). The class of halide perovskites differs from oxide perovskites in having halide anions in place of oxide anions (ABX_3 ; A = monovalent cation, B = divalent metal cation, X = halogen anion). As ionic crystals, halide perovskites have higher ionic crystallinity than oxide perovskites due to strong ionicity of halide anion. In halide perovskites, charge neutralization is established in the lattice structure by the coordination of a large number of cations and anions as mentioned above. Therefore, a slight structural strain due to fluctuations in the distance between ions (or ionic radius) and the coordination number leads to changes in the three-dimensional structure of the crystal. Spatial halide perovskites demonstrate the semiconducting properties and strong visible light absorption desired for photovoltaic applications. The discovery of such halide perovskites dates back to the 1890s. Wells conducted a comprehensive study on the synthesis of lead halide crystals from solutions including cesium Cs-based $CsPbX_3$ (X = Cl, Br, I). Figure *1.2* shows an orange crystal of $CsPbBr_3$. Later, Danish researcher Møller found that $CsPbCl_3$ and $CsPbBr_3$ have a perovskite structure, showing a tetragonally distorted structure that undergoes transition to a pure cubic phase at high temperatures.[5], [22], [23] A simple solution process for the synthesis of these lead halide crystals might
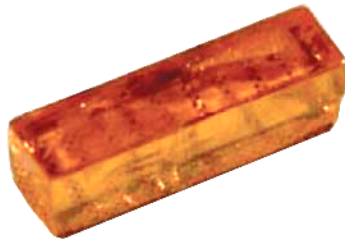

Figure 1.2: Single crystal of lead halide perovkite $CsPbBr_3$ [7]

have inspired researchers to use other cations in place of Cs. Weber found that organic cation CH_3NH_3+ replaces $Cs+$ to form $CH_3NH_3MX_3$ (M = Pb, Sn, X = I, Br) and reported the first crystallographic study on organic–inorganic hybrid lead halide perovskites. Toward the end of the last century, the synthesis of a large variety of halide perovskites composed of small and large organic cations was conducted by David Mitzi. He focused his studies on the physical properties of perovskite materials of low-dimensional structures such as two-dimensional perovskites bearing a large organic group. Although research paved the way to the applications of low-dimensional perovskite crystals to nonlinear optics and electroluminescence by utilizing sharp monochromatic optical absorption and luminescence, at that time, it was not known that these materials could be employed for the utilization of solar energy. This requires a wide spectral absorption to harvest sunlight rather than having a sharp absorption and emission.[6], [24], [25]

2. Theory

[8], [28], [29], [30]

2.1 Carrier-Transport Phenomena

2.1.1 Basic Equations

The basic equations for semiconductor-device operation describe the static and dynamic behavior of carriers in semiconductors under external influences, such as applied field or optical excitation, that cause deviation from the thermal-equilibrium condition.

Current-Density Equations

The current conduction consists of the drift component, caused by the electric field, and the diffusion component, caused by the carrier-concentration gradient. The current-density equations are:

$$J_n = q\mu_n n\mathcal{E} + qD_n\nabla n \tag{2.1}$$

$$J_p = q\mu_p p\mathcal{E} - qD_p\nabla p \tag{2.2}$$

$$J_{cond} = J_n + J_p \tag{2.3}$$

where J_n and J_p are the electron and hole current densities. The values of the electron and hole mobilities (μ_n and μ_p) will be given in section 'Drift and Mobility'. For nondegenerate semiconductors the carrier diffusion constants (D_n and D_p) and the mobilities are given by the Einstein relation $D_n = (kT/q)\mu_p$.

For a one-dimensional case, equations (2.1) and (2.2) reduce to

$$J_n = q\mu_n n\mathcal{E} + qD_n\frac{dn}{dx} = q\mu_n\left(n\mathcal{E} + \frac{kT}{q}\frac{dn}{dx}\right) = \mu_n n\frac{dE_{Fn}}{dx} \tag{2.4}$$

$$J_p = q\mu_p p\mathcal{E} - qD_p\frac{dp}{dx} = q\mu_p\left(p\mathcal{E} + \frac{kT}{q}\frac{dp}{dx}\right) = \mu_p p\frac{dE_{Fp}}{dx} \tag{2.5}$$

where E_{Fn} and E_{Fp} are quasi Fermi levels for electrons and holes. These equations are valid for low electric fields.

Continuity Equations

While the above current-density equations are for steady-state conditions, the continuity equations deal with time-dependent phenomena such as low-level injection, generation and recombination. Qualitatively, the net change of carrier concentration is the difference between generation and recombination, plus the

net current flowing in and out of the region of interest. The continuity equations are:

$$\frac{\partial n}{\partial t} = G_n - U_n + \frac{1}{q}\nabla \cdot J_n \tag{2.6}$$

$$\frac{\partial p}{\partial t} = G_p - U_p + \frac{1}{q}\nabla \cdot J_p \tag{2.7}$$

where G_n and G_p are the electron and hole generation rate, caused by external influences such as the optical excitation with photons or impact ionization under large electric fields, and where $U_n = \nabla n/\tau_n$ and $U_p = \nabla p/\tau_p$ are recombination rates.

For the one-dimensional case under a low-injection condition, equations (2.6) and (2.7) reduce to

$$\frac{\partial n_p}{\partial t} = G_n - \frac{n_p - n_{po}}{\tau_n} + n_p\mu_n\frac{\partial \mathcal{E}}{\partial x} + D_n\frac{\partial^2 n_p}{\partial x^2} \tag{2.8}$$

$$\frac{\partial p_n}{\partial t} = G_p - \frac{p_n - p_{no}}{\tau_p} + p_n\mu_p\frac{\partial \mathcal{E}}{\partial x} + D_p\frac{\partial^2 p_n}{\partial x^2} \tag{2.9}$$

2.1.2 Drift and Mobility

At low electric fields, the drift velocity v_d is proportional to the electric field strength $\mathcal{E}$ and the proportionality constant is defined as the mobility μ, or

$$v_d = \mu\mathcal{E} \tag{2.10}$$

and the electric field is given by

$$\mathcal{E} = \frac{U_z}{l} \tag{2.11}$$

where U_z is the difference of potencials between two zones of the measured sample, and l is the distance between them. For a case where each zone ($z1$ and $z2$) is defined by unique voltage peak, equations above reduce to one-dimensional modifying form

$$v_{z1,z2}t_{z1,z2} = \frac{x_{z1,z2}}{2} \tag{2.12}$$

where extended form of $t_{z1,z2}$ gives $t_{z1} + t_{z2} = \Delta t$ is time difference between voltage peaks of zones. Equation (2.10) then tends to

$$\frac{x_{z1,z2}}{2t_{z1,z2}} = \mathcal{E}_{z1,z2}\mu \tag{2.13}$$

which serves this equation as

$$\frac{x_{z1}}{2\mathcal{E}_{z1}} + \frac{x_{z2}}{2\mathcal{E}_{z2}} = \Delta t\mu \tag{2.14}$$

thus, final expression for mobility determination

$$\mu = \frac{1}{2\Delta t}\left(\frac{x_{z1}}{\mathcal{E}_{z1}} + \frac{x_{z2}}{\mathcal{E}_{z2}}\right) \tag{2.15}$$

2.2   p-n Junctions

2.2.1   Depletion Region

Abrupt Junction

When the impurity concentration in a semiconductor changes abruptly from acceptor impurities N_A to donor impurities N_D, as shown in Figure *2.1a*, one obtains an abrupt junction. In particular, if $N_A \gg N_D$ (or vice versa), one obtains a one-sided abrupt $p^+ - n$ (or $n^+ - p$) junction.

We first consider the thermal equilibrium condition, that is, one without applied voltage and current flow. Then

$$J_n = 0 = q\mu_n\left(n\mathcal{E} + \frac{kT}{q}\frac{dn}{dx}\right) = \mu_n n\frac{dE_F}{dx} \tag{2.16}$$

$$\frac{dE_F}{dx} = 0 \tag{2.17}$$

Similarly

$$J_p = 0 = \mu_p p\frac{dE_F}{dx} = 0 \tag{2.18}$$

Thus the condition of zero net electron and hole currents requires that the Fermi level must be constant throughout the sample. The built-in potential ψ_{bi}, or diffusion potential, as shown in Figure *2.1b,c,d*, is equal to

$$q\psi_{bi} = E_g - (q\phi_n + q\phi_p) = q\psi_{Bn} + q\psi_{Bp} \tag{2.19}$$

For nondegenerate semiconductors,

$$\psi_{bi} \approx \frac{kT}{q}\ln\left(\frac{N_D N_A}{n_i^2}\right) \tag{2.20}$$

Since at equilibrium $n_{no}p_{no} = n_{po}p_{po} = n_i^2$,

$$\psi_{bi} = \frac{kT}{q}\ln\left(\frac{p_{po}}{p_{no}}\right) = \frac{kT}{q}\ln\left(\frac{n_{no}}{n_{po}}\right) \tag{2.21}$$

This gives the relationship between carrier densities on either side of the junction.

Since in thermal equilibrium the electric field in the neutral regions (far from the junction at either side) of the semiconductor must be zero, the total negative charge per unit area in the p-side must be precisely equal to the total positive charge per unit area in the n-side:

$$N_A W_{Dp} = N_D W_{Dn} \tag{2.22}$$

p-region | n-region

|← Depletion region →|

Depletion charge
$(N_D - N_A)$

$\oplus \oplus \oplus \oplus \oplus$ Donor
$\oplus \oplus \oplus \oplus \oplus$ density (N_D)
$\oplus \oplus \oplus \oplus \oplus$

$- W_{Dp}$

$\ominus \ominus \ominus$ 0 W_{Dn} x **(a)**
$\ominus \ominus \ominus$
$\ominus \ominus \ominus$
$\ominus \ominus \ominus$
$\ominus \ominus \ominus$

Acceptor
density (N_A)

$\mathscr{E}$ $- W_{Dp}$ 0 W_{Dn} x **(b)**

Area = built-in
potential ψ_{bi}

$- \mathscr{E}_m$

ψ_i $- \psi_n$ ψ_{bi} **(c)**

ψ_p

0   x

E_C

$q\psi_{bi}$

E_i

$q\phi_p$ $q\psi_{Bp}$ $q\psi_p$ $q\phi_n$ **(d)**
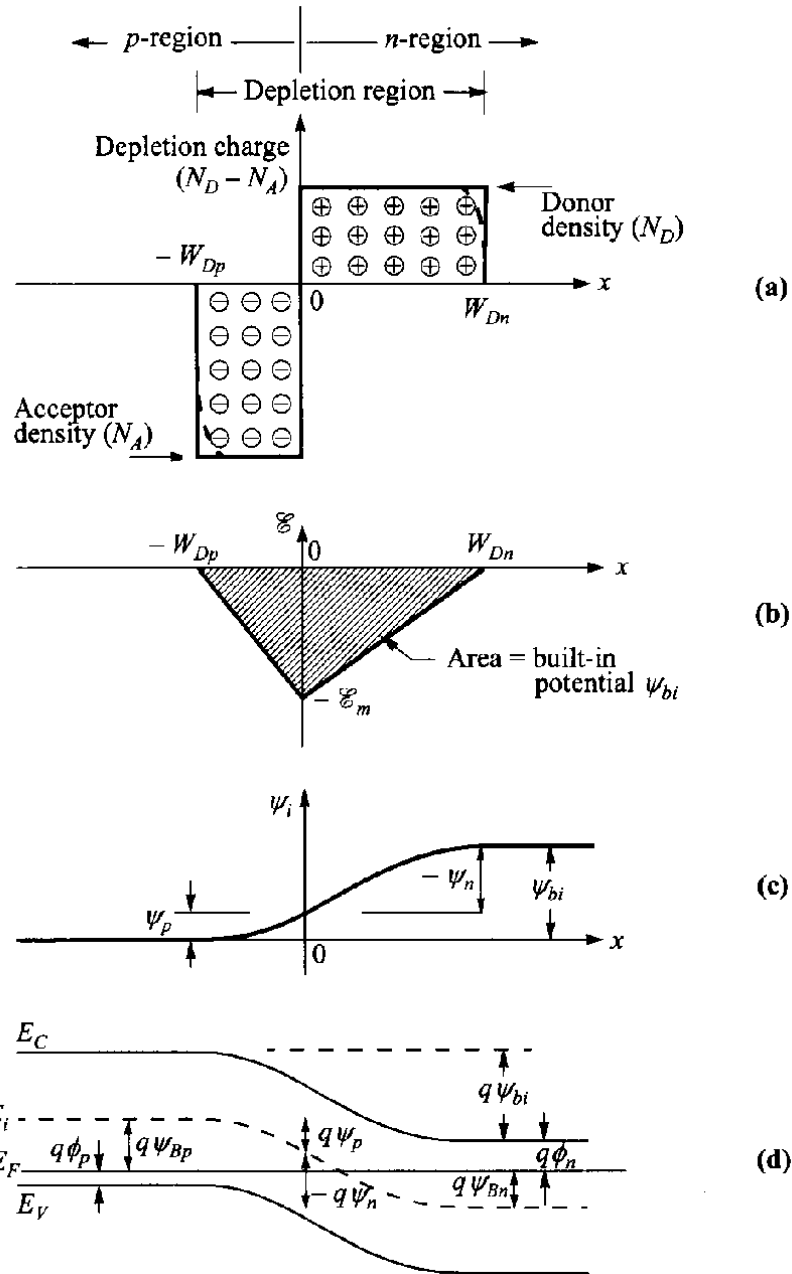
E_F

E_V $-q\psi_n$ $q\psi_{Bn}$

Figure 2.1: Abrupt $p - n$ junction in thermal equilibrium. (a) Space-charge distribution. Dashed lines indicate corrections to depletion approximation. (b) Electric-field distribution. (c) Potential distribution where $\psi_b i$ is the built-in potential. (c) Energy-band diagram.

From the Poisson equation we obtain

$$-\frac{d^2\psi_i}{dx^2} = \frac{d\mathcal{E}}{dx} = \frac{\rho(x)}{\varepsilon_s} = \frac{q}{\varepsilon_s}\left[N_D^+(x) - n(x) - N_A^-(x) + p(x)\right] \quad (2.23)$$

Inside the depletion region, $n(x) = p(x) = 0$,

$$\begin{aligned}
\frac{d^2\psi_i}{dx^2} &\approx \frac{qN_A}{\varepsilon_s} \qquad &&\text{for} \qquad -W_{Dp} \le x \le 0 \\
-\frac{d^2\psi_i}{dx^2} &\approx \frac{qN_D}{\varepsilon_s} \qquad &&\text{for} \qquad 0 \le x \le W_{Dn}
\end{aligned} \qquad (2.24)$$

The electric field is then obtained by integrating the above equations, as shown in Figure *2.1b*:

$$\mathcal{E}(x) = \frac{qN_A(x + W_{Dp})}{\varepsilon_s} \qquad \text{for} \qquad -W_{Dp} \le x \le 0 \qquad (2.25)$$

$$\mathcal{E}(x) = -\mathcal{E}_m + \frac{qN_D x}{\varepsilon_s} = -\frac{qN_D}{\varepsilon_s}(W_{Dn} - x) \qquad \text{for} \qquad 0 \le x \le W_{Dn} \qquad (2.26)$$

where $\mathcal{E}_m$ is the maximum field that exists at $x = 0$ and is given by

$$|\mathcal{E}_m| = \frac{qN_D W_{Dn}}{\varepsilon_s} = \frac{qN_A W_{Dp}}{\varepsilon_s} \qquad (2.27)$$

Integrating equation (2.25) and (2.26) once again gives the potential distribution $\psi_i(x)$ (Figure *2.1c*)

$$\psi_i(x) = \frac{qN_A}{\varepsilon_s}(x + W_{Dp})^2 \qquad \text{for} \qquad -W_{Dp} \le x \le 0 \qquad (2.28)$$

$$\psi_i(x) = \psi_i(0) + \frac{qN_D}{\varepsilon_s}\left(W_{Dn} - \frac{x}{2}\right)x \qquad \text{for} \qquad 0 \le x \le W_{Dn} \qquad (2.29)$$

With these, the potentials across different regions can be found as

$$\psi_p = \frac{qN_A W_{Dp}^2}{2\varepsilon_s} \qquad (2.30)$$

$$|\psi_n| = \frac{qN_D W_{Dn}^2}{2\varepsilon_s} \qquad (2.31)$$

then

$$\psi_{bi} = \psi_p + |\psi_n| = \psi_i(W_{Dn}) = \frac{|\mathcal{E}_m|}{2}(W_{Dp} + W_{Dn}) \qquad (2.32)$$

where $\mathcal{E}_m$ can also be expressed as

$$|\mathcal{E}_m| = \sqrt{\frac{2qN_A\psi_p}{\varepsilon_s}} = \sqrt{\frac{2qN_D\psi_n}{\varepsilon_s}} \qquad (2.33)$$

The depletion widths are calculated to be

$$W_{Dp} = \sqrt{\frac{2\varepsilon_s \psi_{bi}}{q} \frac{N_D}{N_A(N_A + N_D)}} \tag{2.34}$$

$$W_{Dn} = \sqrt{\frac{2\varepsilon_s \psi_{bi}}{q} \frac{N_A}{N_D(N_A + N_D)}} \tag{2.35}$$

$$W_{Dp} + W_{Dn} = \sqrt{\frac{2\varepsilon_s}{q} \left(\frac{N_A + N_D}{N_A N_D}\right) \psi_{bi}} \tag{2.36}$$

The following relationships can be deduced

$$\frac{|\psi_n|}{\psi_{bi}} = \frac{W_{Dn}}{W_{Dp} + W_{Dn}} = \frac{N_A}{N_A + N_D} \tag{2.37}$$

$$\frac{\psi_p}{\psi_{bi}} = \frac{W_{Dp}}{W_{Dp} + W_{Dn}} = \frac{N_D}{N_A + N_D} \tag{2.38}$$

2.2.2 Current-Voltage Characteristics

Ideal Case - Shockley Equation

The ideal current-voltage characteristics are based on the following four assumptions: (1) the abrupt depletion-layer approximation; that is, the built-in potential and applied voltages are supported by a dipole layer with abrupt boundaries, and outside the boundaries the semiconductor is assumed to be neutral; (2) the Boltzmann approximation is valid; (3) the low-injection assumption; that is, the injected minority carrier densities are small compared with the majority-carrier densities; and (4) no generation-recombination current exists inside the depletion layer, and the electron and hole currents are constant throughout the depletion layer.

We first consider the Boltzmann relation. At thermal equilibrium this relation is given by

$$n = n_i \exp\left(\frac{E_F - E_i}{kT}\right) \tag{2.39}$$

$$p = n_i \exp\left(\frac{E_i - E_F}{kT}\right) \tag{2.40}$$

At thermal equilibrium, the pn product from the above equations is equal to n_i^2. When voltage is applied, the minority-carrier densities on both sides of the junction are changed, and the pn product is no longer equal to n_i^2. We define the quasi-Fermi levels as follows

$$n \equiv n_i \exp\left(\frac{E_{Fn} - E_i}{kT}\right) \tag{2.41}$$

$$p \equiv n_i \exp\left(\frac{E_i - E_{Fp}}{kT}\right) \tag{2.42}$$

where E_{Fn} and E_{Fp} are the quasi-Fermi levels for electrons and holes. From equations (2.41) and (2.42) we obtain

$$E_{Fn} \equiv E_i + kT \ln \left(\frac{n}{n_i} \right) \tag{2.43}$$

$$E_{Fp} \equiv E_i + kT \ln \left(\frac{p}{n_i} \right) \tag{2.44}$$

The *pn* product becomes

$$pn = n_i^2 \exp \left(\frac{E_{Fn} + E_{Fp}}{kT} \right) \tag{2.45}$$

For a forward bias, $(E_{Fn} + E_{Fp}) > 0$ and $pn > n_i^2$, for a reversed bias, $(E_{Fn} + E_{Fp}) < 0$ and $pn < n_i^2$. From equations (2.4),(2.41) and the fact that $\mathcal{E} \equiv \nabla E_i / q$ we obtain

$$
\begin{aligned}
J_n &= q\mu_n \left(n\mathcal{E} + \frac{kT}{q} \nabla n \right) = \mu_n n \nabla E_i + \mu_n kT \left[\frac{n}{kT} (\nabla E_{Fn} - \nabla E_i) \right] \\
&= \mu_n n \nabla E_{Fn}
\end{aligned}
\tag{2.46}
$$

Similarly, we obtain

$$J_p = \mu_p p \nabla E_{Fp} \tag{2.47}$$

Thus, the electron and hole current densities are proportional to the gradients of the electron and hole quasi-Fermi levels, respectively. If $E_{Fn} = E_{Fp} = $ constant (at thermal equilibrium), then $J_n = J_p = 0$.

The idealized potential distributions and the carrier concentrations in a $p - n$ junction under forward-bias and reverse-bias conditions are shown in Figure *2.2*. The variations of E_{Fn} and E_{Fp} with distance are related to the carrier concentrations as given in equations (2.43) and (2.44), and to the current as given by equations (2.46) and (2.47). Inside the depletion region, E_{Fn} and E_{Fp} remain relatively constant. This comes about because the carrier concentrations are relatively much higher inside the depletion region, but since the currents remain fairly constant, the gradients of the quasi-Fermi levels have to be small. In addition, the depletion width is typically much shorter than the diffusion length, so the total drop of quasi-Fermi levels inside the depletion width is not significant. With these arguments, it follows that within the depletion region

$$qV = E_{Fn} - E_{Fp} \tag{2.48}$$

Equations (2.45) and (2.48) can be combined to give the electron density at the boundary of the depletion-layer region on the p-side ($x = -W_{Dp}$):

$$n_p(-W_{Dp}) = \frac{n_i^2}{p_p} \exp \left(\frac{qV}{kT} \right) \approx n_{po} \exp \left(\frac{qV}{kT} \right) \tag{2.49}$$

where $p_p \approx p_{po}$ for low-level injection, and n_{po} is the equilibrium electron density on the p-side. Similarly

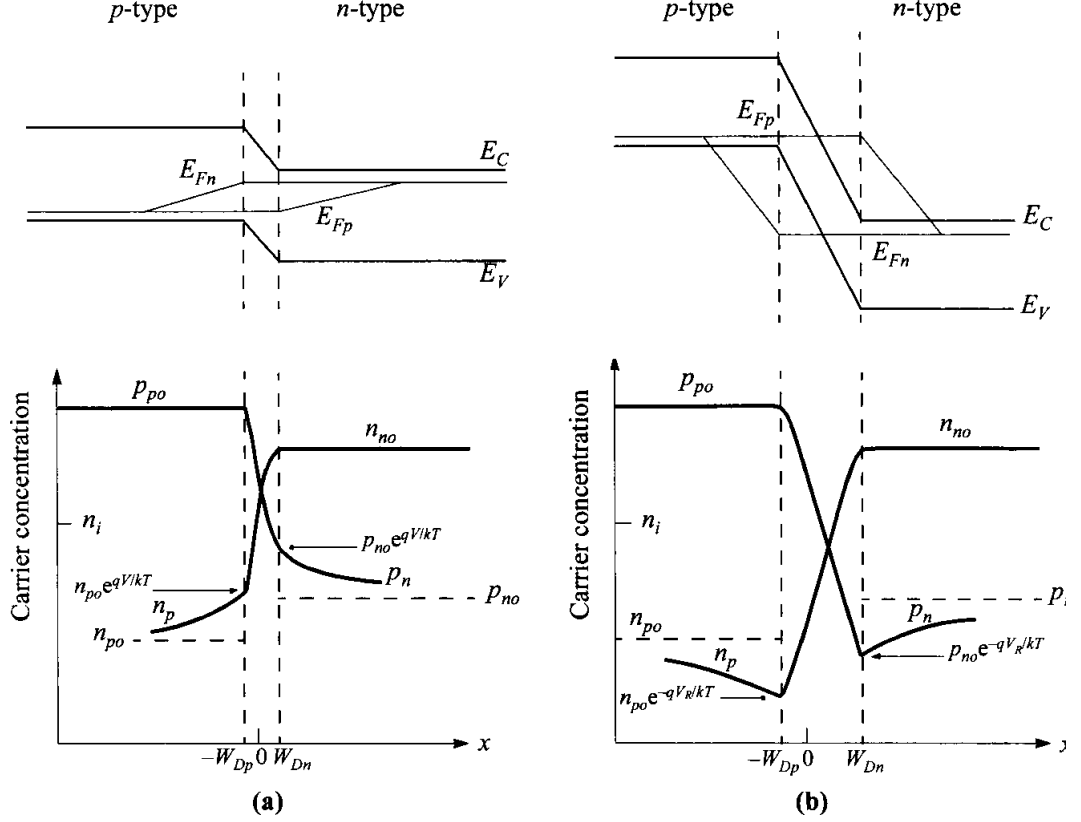$$p_n(W_{Dn}) = p_{no} \exp \left(\frac{qV}{kT} \right) \tag{2.50}$$

11

Figure 2.2: Energy-band diagram, with quasi-Fermi levels for electrons and holes, and carrier distributions under (a) forward bias and (b) reverse bias.

at $x = W_{Dn}$ for the n-type boundary. The preceding equations are the most-important boundary conditions for the ideal current-voltage equation.

From the continuity equations we obtain for the steady-state condition in the n-side of the junction:

$$-U + \mu_n \mathcal{E} \frac{dn_n}{dx} + \mu_n n_n \frac{\mathcal{E}}{dx} + D_n \frac{d^2 n_n}{dx^2} = 0 \tag{2.51}$$

$$-U - \mu_p \mathcal{E} \frac{dp_n}{dx} - \mu_p p_n \frac{\mathcal{E}}{dx} + D_p \frac{d^2 p_n}{dx^2} = 0 \tag{2.52}$$

In these equations, U is the net recombination rate. Multiplying (2.51) by $\mu_p p_n$ and (2.52) by $\mu_n n_n$, and combining with the Einstein relation $D = (kT/q)\mu$, we obtain

$$-\frac{p_n - p_{no}}{\tau_p} - \frac{n_n - p_n}{(n_n/\mu_n) + (p_n/\mu_n)} \frac{\mathcal{E} dp_n}{dx} + D_a \frac{d^2 p_n}{dx^2} = 0 \tag{2.53}$$

where

$$D_a = \frac{n_n + p_n}{n_n/D_p + p_n/D_n} \tag{2.54}$$

is the ambipolar diffusion coefficient, and

$$\tau_p \equiv \frac{p_n - p_{no}}{U} \tag{2.55}$$

12

From the low-injection assumption equation (2.53) reduces to

$$-\frac{p_n - p_{no}}{\tau_p} - \mu_p \mathcal{E} \frac{dp_n}{dx} + D_a \frac{d^2 p_n}{dx^2} = 0 \tag{2.56}$$

In the neutral region where there is no electric field, equation (2.56) further reduces to

$$\frac{d^2 p_n}{dx^2} - \frac{p_n - p_{no}}{D_p \tau_p} = 0 \tag{2.57}$$

The solution of equation (2.57), with the boundary conditions of (2.50) and $p_n(x = \infty) = P_{no}$, gives

$$p_n(x) - p_{no} = p_{no} \left[\exp\left(\frac{qV}{kT}\right) - 1 \right] \exp\left(-\frac{x - W_{Dn}}{L_p}\right) \tag{2.58}$$

where

$$L_p \equiv \sqrt{D + p\tau_p} \tag{2.59}$$

At $x = W_{Dn}$, the hole diffusion current is

$$J_p = -qD_p \frac{dp_n}{dx}\bigg|_{W_{Dn}} = \frac{qD_p p_{no}}{L_p} \left[\exp\left(\frac{qV}{kT}\right) - 1 \right] \tag{2.60}$$

Similarly, we obtain the electron diffusion current in the p-side

$$J_n = qD_n \frac{dn_p}{dx}\bigg|_{-W_{Dp}} = \frac{qD_n n_{po}}{L_n} \left[\exp\left(\frac{qV}{kT}\right) - 1 \right] \tag{2.61}$$

The total current is given by the sum of equations (2.60) and (2.61):

$$J = J_p + J_n = J_0 \left[\exp\left(\frac{qV}{kT}\right) - 1 \right] \tag{2.62}$$

which is Shockley equation (also ideal didode law), where the saturation current density J_0 is used.

The Shockley equation adequately predicts the current-voltage characteristics of germanium $p-n$ junctions at low current densities. For $p-n$ junctions of other materials, the ideal equation can only give qualitative agreement. The departures from the ideal are mainly due to: (1) the generation and recombination of carriers in the depletion layer, (2) the high-injection condition that may occur even at relatively small forward bias, (3) the parasitic IR drop due to series resistance, (4) the tunneling of carriers between states in the bandgap, and (5) the surface effects.

The surface effects on $p-n$ junctions are primarily due to ionic charges on or outside the semiconductor surface that induce image charges in the semiconductor, and thereby cause the formation of the so-called surface channels or surface depletion-layer regions. Once a channel is formed, it modifies the junction depletion region and gives rise to surface leakage current.

2.3 Metal-Semiconductor Contacts

2.3.1 Introduction

Schottky suggested that the potential barrier could arise from stable space charges in the semiconductor alone without the presence of a chemical layer. The model arising from this consideration is known as the Schottky barrier. Mott also devised a more appropriate theoretical model for swept-out metal-semiconductor contacts that is known as the Mott barrier. Ideas about the role of the space charge in determining the shape of the barrier were advanced by Davydov.

2.3.2 Formation of Barrier

When metal makes contact with a semiconductor, a barrier is formed at the metal-semiconductor interface. This barrier is responsible for controlling the current conduction as well as its capacitance behavior. Consider the basic energy-band diagrams leading to the formation of the barrier height and some effects that can modify the value of this barrier.

Ideal Condition

Consider the ideal case without surface states and other anomalies. Figure *2.3* shows the electronic energy relations of a high work function metal and an n-type semiconductor which are not in contact and are in separate systems. If the two are allowed to communicate with each other charge will flow from the semiconductor to the metal and thermal equilibrium is established as a single system. The Fermi levels on both sides will line up. Relative to the Fermi level in the metal, the Fermi level in the semiconductor is lowered by an amount equal to the difference between the two work functions.
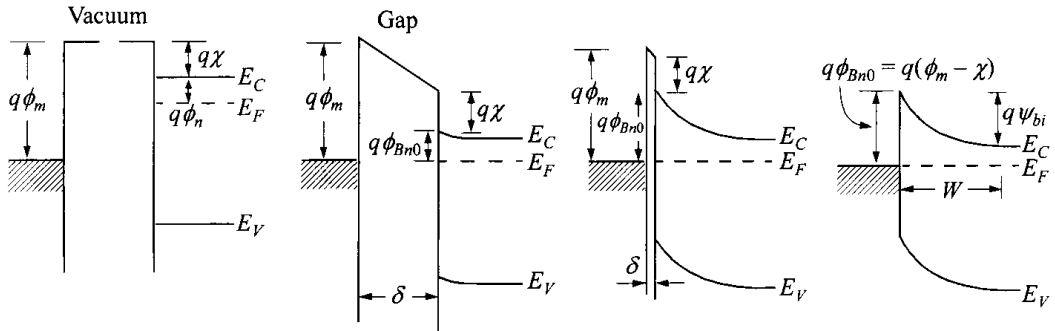

Figure 2.3: Energy-band diagrams of metal-semiconductor contacts. Metal and semiconductor (a) in separated systems, and (b) connected into one system. As the gap δ (c) is reduced and (d) becomes zero.

The work function is the energy difference between the vacuum level and the Fermi level. This quantity is denoted by $q\phi_m$ for the metal, and is equal to $q(\chi + \phi_n)$ in the semiconductor, where $q\chi$ is the electron affinity measured from the bottom of the conduction band E_c to the vacuum level, and $q\phi_n$ is the energy difference between E_c and the Fermi level. The potential difference between the two work functions $\phi_m - (\chi + \phi_n)$ is called the contact potential.

As the gap distance δ decreases, the electric field in the gap increases and an increasing negative charge is built up at the metal surface. An equal and opposite charge (positive) must exist in the semiconductor depletion region. The potential variation within the depletion layer is similar to that in one side of a $p-n$ junction. When δ is small enough to be comparable to the inter-atomic distances, the gap becomes transparent to electrons, and we obtain the limiting case, as shown on Figure 2.1d. It is clear that the limiting value of the barrier height $q\phi_{Bn0}$ is given by

$$q\phi_{Bn0} = q(\phi_m - \chi) \tag{2.63}$$

The barrier height is the difference between the metal work function and the electron affinity of the semiconductor. Conversely, for an ideal contact between a metal and a p-type semiconductor, the barrier height $q\phi_{Bn0}$ is given by

$$q\phi_{Bp0} = E_g - q(\phi_m - \chi) \tag{2.64}$$

For any given semiconductor and metal combination, the sum of the barrier heights on n-type and p-type substrates is expected to be equal to the bandgap, or

$$E_g = q(\phi_{Bn0} + \phi_{Bp0}) \tag{2.65}$$

Depletion Layer

The depletion layer of a metal-semiconductor contact is similar to that of the onesided abrupt (p^+-n) junction. When a metal is brought into intimate contact with a semiconductor, the conduction and valence bands of the semiconductor at the surface are brought into a definite energy relationship with the Fermi level in the metal. Once this relationship is established, it serves as a boundary condition to the solution of the Poisson equation in the semiconductor, which proceeds in exactly the same manner as in a $p-n$ junction. The energy-band diagrams for metals on both n-type and p-type materials are shown, under different biasing conditions, in Figure *2.4*.

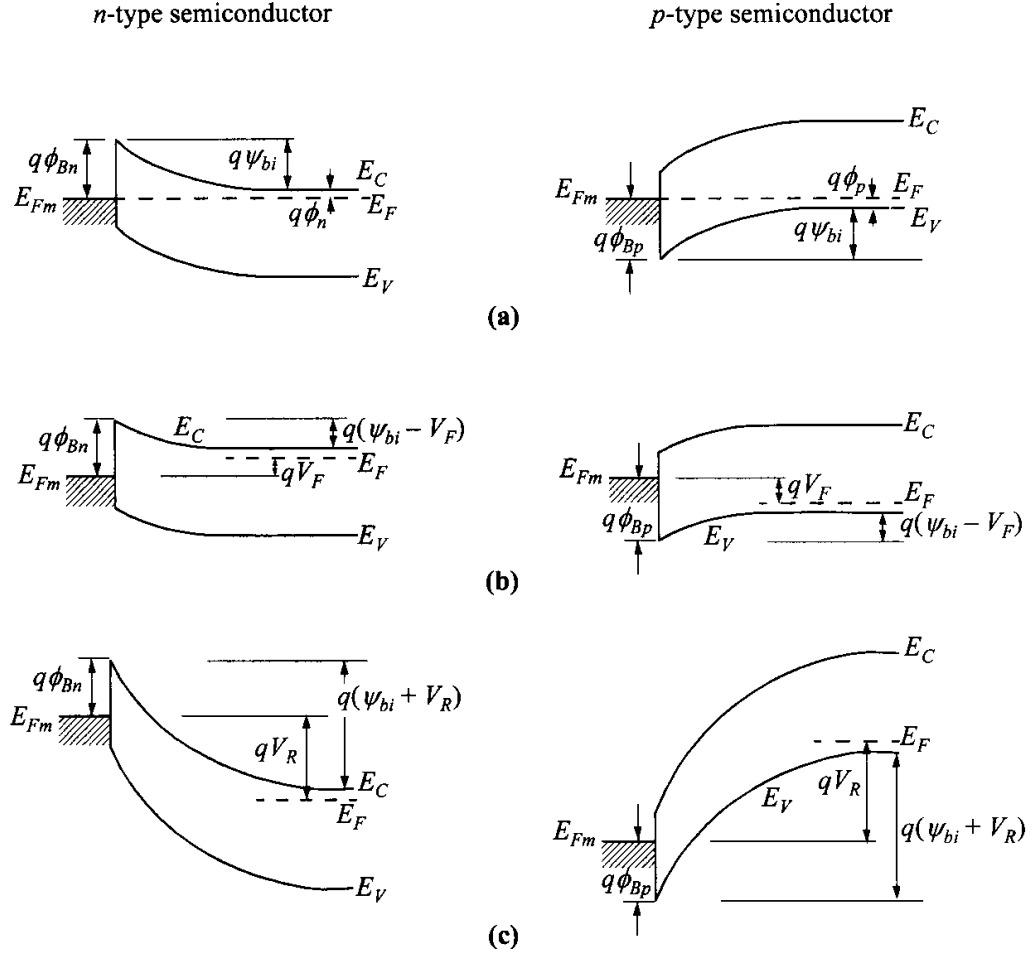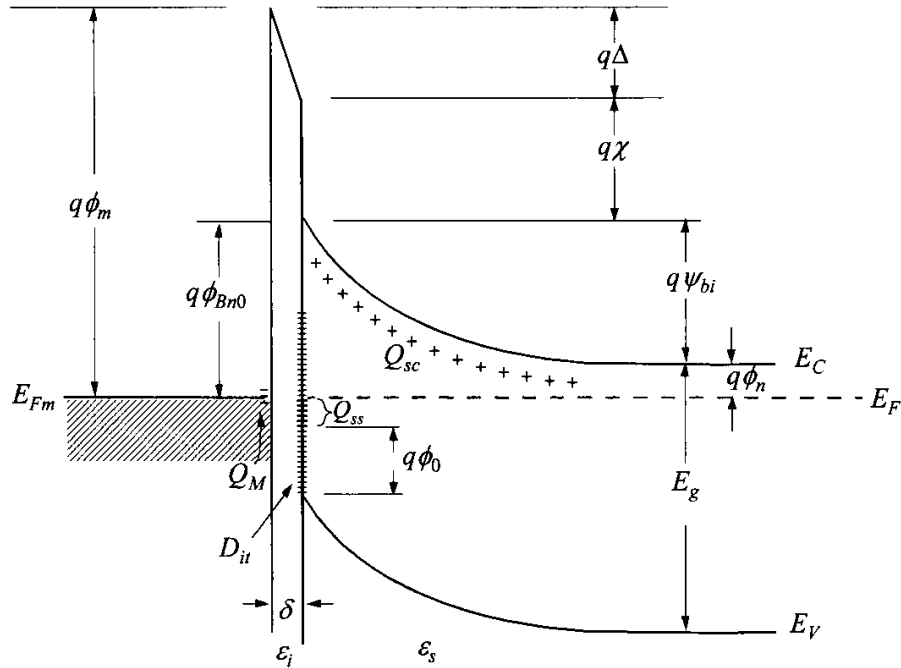*n*-type semiconductor   *p*-type semiconductor

(a)

(b)

(c)

Figure 2.4: Energy-band diagrams of metal on n-type (left) and p-type (right) semiconductors under different biasing conditions. (a) Thermal equilibrium. (b) Forward bias. (c) Reverse bias.

Interface States

The barrier heights of metal-semiconductor systems are determined by both the metal work function and the interface states. A general expression of the barrier height can be obtained on the basis of the following two assumption: with intimate contact between the metal and the semiconductor, and with an interfacial layer of atomic dimensions, this layer will be transparent to electrons but can withstand potential across it, and the interface states per unit area per energy at the interface are a property of the semiconductor surface and are independent of the metal.

A more detailed energy-band diagram of a practical metal-*n*-semiconductor contact is shown in Figure *2.5*. The various quantities used in the derivation that follows are defined in this figure. The first quantity of interest is the energy level $q\phi_0$ above E_V, at the semiconductor surface. It is called the neutral level above which the states are of acceptor type (neutral when empty, negatively charged when full) and below which the states are of donor type (neutral when full of electrons, positively charged when empty). Consequently, when the Fermi level at the surface coincides with this neutral level, the net interface-trap charge is

zero. This energy level also tends to pin the semiconductor Fermi level at the surface before the metal contact was formed.

ϕ_m = Work function of metal
ϕ_{Bn0} = Barrier height (without image-force lowering)
ϕ_0 = Neutral level (above E_V) of interface states
Δ = Potential across interfacial layer
χ = Electron affinity of semiconductor
ψ_{bi} = Built-in potential
δ = Thickness of interfacial layer
Q_{sc} = Space-charge density in semiconductor
Q_{ss} = Interface-trap charge
Q_M = Surface-charge density on metal
D_{it} = Interface-trap density
ε_i = Permittivity of interfacial layer (vacuum)
ε_s = Permittivity of semiconductor

Figure 2.5: Detailed energy-band diagram of a metal-n-semiconductor contact with an interfacial layer (vacuum) of the order of atomic distance

The second quantity is $q\phi_{Bn0}$, the barrier height of the metal-semiconductor contact, it is this barrier that must be surmounted by electrons flowing from the metal into the semiconductor. The interfacial layer will be assumed to have a thickness of a few angstroms and will therefore be essentially transparent to electrons.

Consider a semiconductor with acceptor interface traps (since in this particular example E_F is above the neutral level) whose density is D_{it} states/cm^2-eV, and is a constant over the energy range from $q\phi_0 + E_V$ to the Fermi level. The interface-trap charge density on the semiconductor Q_{ss} is therefore negative and

is given by

$$Q_{ss} = -qD_{it}(E_g - q\phi_0 - q\phi_{Bn0}) \tag{2.66}$$

The quantity in parentheses is simply the energy difference between the Fermi level at the surface and the neutral level. The interface-trap density D_{it} times this quantity yields the number of surface states above the neutral level that are full.

The space charge that forms in the depletion layer of the semiconductor at thermal equilibrium is given as

$$Q_{sc} = qN_DW_D = \sqrt{2q\varepsilon_S N_D \left(\phi_{Bn0} - \phi_n - \frac{kT}{q}\right)} \tag{2.67}$$

In the absence of any space-charge effects in the interfacial layer, an exactly equal and opposite charge, Q_M, develops on the metal surface. For thin interfacial layers such space-charge effects are negligible and Q_M can be written as

$$Q_M = -(Q_{ss} + Q_{sc}) \tag{2.68}$$

The potential Δ across the interfacial layer can be obtained by applying Gauss'law to the surface charge on the metal and semiconductor by

$$\Delta = -\frac{\delta Q_M}{\varepsilon_i} \tag{2.69}$$

where ε_i is the permittivity of the interfacial layer and δ its thickness. Another relation for Δ can be obtained by inspection of the energy-band diagram of Figure 2.3

$$\Delta = \phi_m - (\chi + \phi_{Bn0}) \tag{2.70}$$

This relation results from the fact that the Fermi level must be constant throughout this system at thermal equilibrium.

If Δ is eliminated from equations (2.69) and (2.70), and (2.68) is used to substitute for Q_M, we obtain

$$\phi_m - \chi - \phi_{Bn0} = \sqrt{\frac{2q\varepsilon_S N_D \delta^2}{\varepsilon_i^2}\left(\phi_{Bn0} - \phi_n - \frac{kT}{q}\right)} - \frac{qD_{it}\delta}{\varepsilon_i}(E_g - q\phi_0 - q\phi_{Bn0}) \tag{2.71}$$

Equation (2.71) can now be solved for ϕ_{Bn0}. We introduce the quantities

$$c_1 = \frac{2q\varepsilon_S N_D \delta^2}{\varepsilon_i^2} \tag{2.72}$$

$$c_2 = \frac{\varepsilon_i}{\varepsilon_i + q^2 \delta D_{it}} \tag{2.73}$$

which contain all the interfacial properties. Equation (2.72) can be used to calculate c_1 if values of δ and ε_i are estimated. Neglecting square-root term in (2.71) it reduces to

$$\phi_{Bn0} = c_2(\phi_m - \chi) + (1 - c_2)\left(\frac{E_g}{q} - \phi_0\right) \equiv c_2\phi_m + c_3 \tag{2.74}$$

With known c_2 and c_3 from experiments of varying ϕ_m, the interfacial properties are given by

$$\phi_0 = \frac{E_g}{q} - \frac{c_2\chi + c_3}{1 - c_2} \tag{2.75}$$

$$D_{it} = \frac{(1 - c_2)\varepsilon_i}{c_2\delta q^2} \tag{2.76}$$

There are two limiting cases which can be obtained directly from equation (2.74):
When $D_{it} \to \infty$, then $c_2 \to 0$ and

$$q\phi_{Bn0} = E_g - q\phi_0 \tag{2.77}$$

In this case the Fermi level at the interface is pinned by the surface states at the value $q\phi_0$ above the valence band. The barrier height is independent of the metal work function and is determined entirely by the surface properties of the semiconductor.
When $D_{it} \to 0$, then $c_2 \to 1$ and

$$q\phi_{Bn0} = q(\phi_M - \chi) \tag{2.78}$$

This equation for the barrier height of an ideal Schottky barrier where surface state effects are neglected, is identical to equation (2.63).

Schottky effect

Also Schottky-barrier lowering, is the image-force-induced lowering of the barrier energy for charge carrier emission, in the presence of an electric field. Consider a metal-vacuum system first. The minimum energy necessary for an electron to escape into vacuum from an initial energy at the Fermi level is the work function $q\phi_m$ as shown in Figure *2.6*.

When an electron is at a distance x from the metal, a positive charge will be induced on the metal surface. The force of attraction between the electron and the induced positive charge is equivalent to the force that would exist between the electron and an equal positive charge located at $-x$. This positive charge is referred to as the image charge. The attractive force toward the metal, called the image force, is given by

$$F = \frac{-q^2}{4\pi\varepsilon_0(2x)^2} = \frac{-q^2}{16\pi\varepsilon_0 x^2} \tag{2.79}$$

where ε_0, is the permittivity of free space. The work done to an electron in the course of its transfer from infinity to the point x is given by

$$E(x) = \int_\infty^x F dx = \frac{-q^2}{16\pi\varepsilon_0 x} \tag{2.80}$$

This energy corresponds to the potential energy of an electron placed at a distance x from the metal surface, shown in Figure *2.6*, and is measured downwards from the x-axis. When an external field $\mathcal{E}$ is applied (in this example in the $-x$
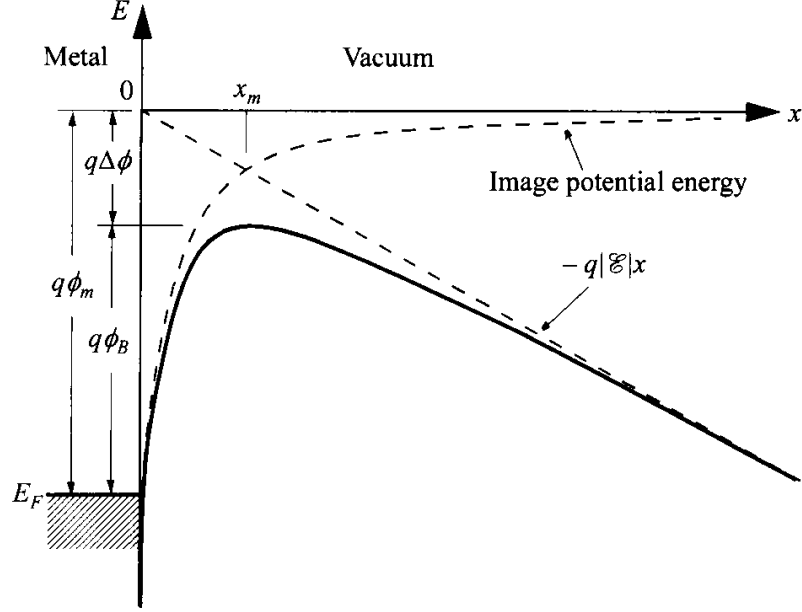
Figure 2.6: Energy-band diagram between a metal surface and a vacuum. The metal work function is $q\phi_m$. The effective barrier is lowered when an electric field is applied to the surface. The lowering is due to the combined effects of the field and the image force.

direction), the total potential energy PE as a function of distance is given by the sum

$$PE(x) = -\frac{q^2}{16\pi\varepsilon_0 x} - q|\mathcal{E}|x \qquad (2.81)$$

This equation has a maximum value. The image-force lowering $\Delta\phi$ and the location of the lowering x_m, (as shown in Figure 2.6), are given by the condition $d(PE)/dx = 0$, or

$$x_m = \sqrt{\frac{q}{16\pi\varepsilon_0|\mathcal{E}|}} \qquad (2.82)$$

$$\Delta\phi = \sqrt{\frac{q|\mathcal{E}|}{4\pi\varepsilon_0}} = 2|\mathcal{E}|x_m \qquad (2.83)$$

The field should be replaced by the appropriate field at the interface, and the free-space permittivity ε_0 should be replaced by an appropriate permittivity ε_s, characterizing the semiconductor medium, that is

$$\Delta\phi = \sqrt{\frac{q\mathcal{E}_m}{4\pi\varepsilon_s}} \qquad (2.84)$$

Inside a device such as metal-semiconductor contact, the field is not zero even without bias due to the built-in potential. Because of the larger values of ε_s, in a metal-semiconductor system, the barrier lowering is smaller than that in a corresponding metal-vacuum system.

In a practical Schottky-barrier diode, the electric field is not constant with distance, and the maximum value at the surface based on the depletion approximation can be used

$$\mathcal{E}_m = \sqrt{\frac{2qN|\Psi_s|}{\varepsilon_s}} \qquad (2.85)$$

where the surface potential ε_s, (on n-type substrate) is

$$|\Psi_s| = \phi_{Bn0} - \phi_n + V_R \tag{2.86}$$

Substituting $\mathcal{E}_m$ into equation (2.84) gives

$$\Delta\phi = \sqrt{\frac{q\mathcal{E}_m}{4\pi\varepsilon_s}} = \left[\frac{q^3 N |\Psi_s|}{8\pi^2 \varepsilon_s^3}\right]^{1/4} \tag{2.87}$$

Figure 2.7 shows the energy diagram incorporating the Schottky effect for a metal on n-type semiconductor under different biasing conditions.
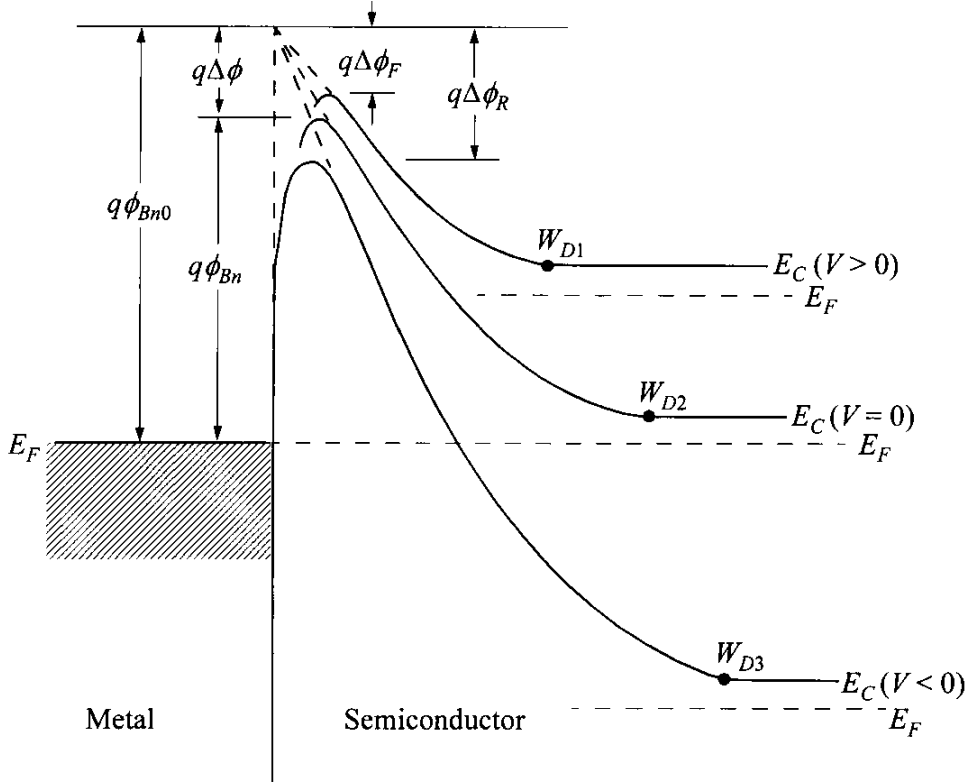

Figure 2.7: Energy-band diagram incorporating the Schottky effect for a metal n-type semiconductor contact under different biasing conditions. The intrinsic barrier height is $q\phi_{Bn0}$. The barrier height at thermal equilibrium is $q\phi_{Bn}$. The barrier lowerings under forward and reverse bias are $\Delta\phi_F$ and $\Delta\phi_R$ respectively.

Barrier Height Adjustment

For an ideal Schottky barrier, the barrier height is determined primarily by the characters of the metal and the metal-semiconductor interface properties and is nearly independent of the doping. Usual Schottky barriers on a given semiconductor (n-type or p-type) therefore give a finite number of choices for barrier height. However, by introducing a thin layer ($= 10$ nm or less) of controllable number of dopants on a semiconductor surface (by ion implantation), the effective barrier height for a given metal-semiconductor contact can be varied. This approach is particularly useful in order to select a metal having the most desirable

metallurgical properties required for reliable device operation and at the same time to be able to adjust the effective barrier height between this metal and the semiconductor in a controlled manner.

Figure *2.8* shows the idealized controlled barrier contacts with a thin n^+-layer or a thin p^+-layer on an n-type substrate for barrier reduction or barrier increase, respectively. Consider the reduction of barrier first.
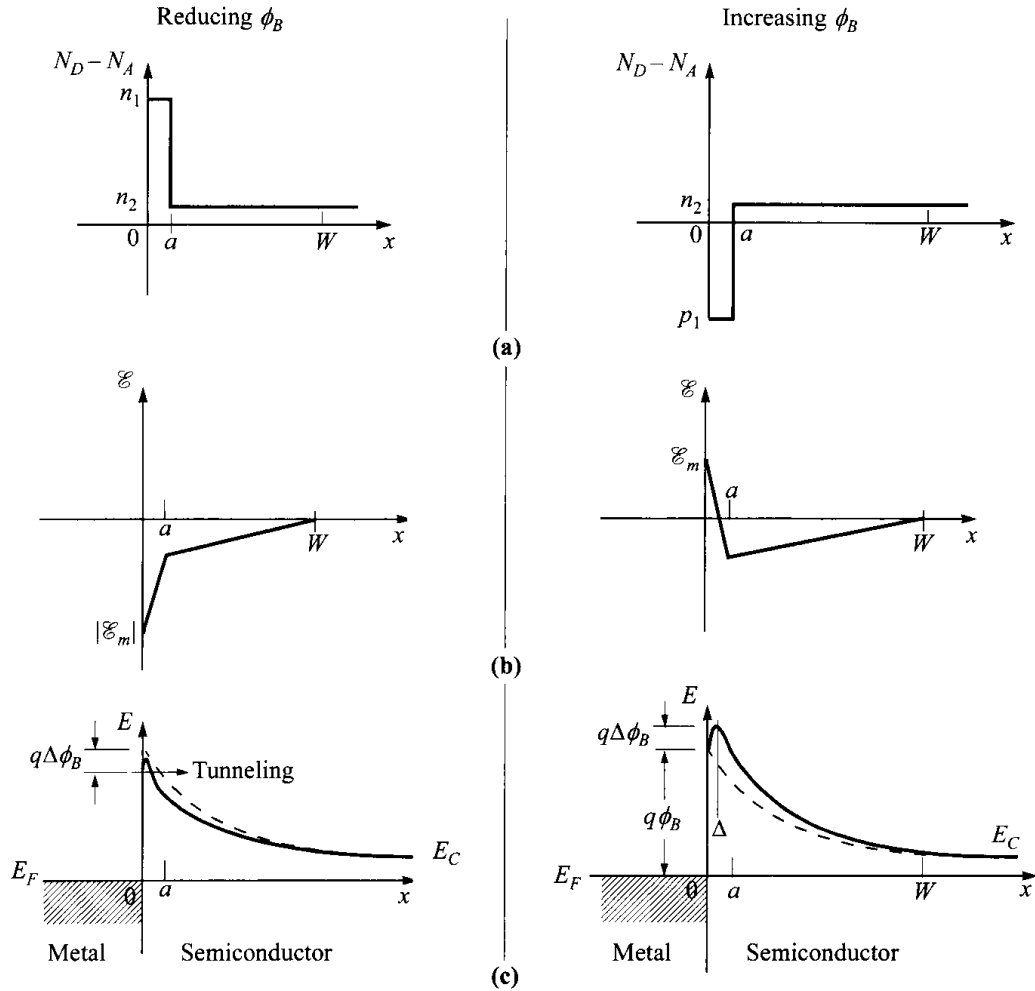
Figure 2.8: Idealized controlled barrier contacts with a thin n^+-layer or a thin p^+-layer on an n-type substrate for barrier reduction (left) or barrier increase (right). Dashed lines indicate original barrier with uniform doping.

The field distribution in Figure *2.8* is given by

$$\mathcal{E} = -|\mathcal{E}_m| + \frac{qn_1 x}{\varepsilon_s} \qquad \text{for} \qquad 0 < x < a$$

$$\mathcal{E} = -\frac{qn_2}{\varepsilon_s}(W - x) \qquad \text{for} \qquad a < x < W \tag{2.88}$$

for $0 < x < a$ where $\mathcal{E}_m$ is the maximum electric field at the metal-semiconductor interface, and is given by

$$|\mathcal{E}_m| = \frac{q}{\varepsilon_s}[n_1 a + n_2(W - a)] \tag{2.89}$$

The image-force lowering due to $\mathcal{E}_m$ is given by equation (2.87). Although the image-force lowering contributes to the barrier reduction, generally the tunneling effect is more significant. For an application parameters n_1 and a should be properly chosen so that in the forward direction the larger Schottky-barrier lowering and the added tunneling current will not substantially degrade the ideality factor η. And in the reverse direction, they will not cause large leakage current in the required bias range. If opposite doping is formed in the thin semiconductor layer at the interface, the effective barrier can be increased. As indicated in Figure *2.8*, if the n^+-region is replaced by p^+-region, it can be shown that the energy-band profile will be $q\phi_B$ at $x = 0$ and reach a maximum at $x = \Delta$, where

$$\Delta = \frac{1}{p_1}[ap_1 - (Q - a)n_2] \tag{2.90}$$

The effective barrier height occurs at $x = \Delta$ and is given by

$$\phi_B' = \phi_B + \mathcal{E}_m\Delta - \frac{qp_1\Delta^2}{2\varepsilon_s} \tag{2.91}$$

Equation (2.91) approaches $\phi_B + qp_1 a^2/2\varepsilon_s$ if $p_1 \gg n_2$ and $ap_1 \gg Wn_2$. Therefore, as the product ap_1 increases, the effective barrier height will increase accordingly.

2.3.3   Current Transport Processes

The current transport in metal-semiconductor contacts is due mainly to majority carriers, in contrast to $p - n$ junctions where the minority carriers are responsible. Figure *2.9* shows five basic transport processes under forward bias (the inverse processes occur under reverse bias). These five processes are (1) emission of electrons from the semiconductor over the potential barrier into the metal, (2) quantum-mechanical tunneling of electrons through the barrier (important for heavily doped semiconductors and responsible for most ohmic contacts), (3) recombination in the space-charge region (identical to the recombination process in a $p - n$ junction), (4) diffusion of electrons in the depletion region, and (5) holes injected from the metal that diffuse into the semiconductor (equivalent to recombination in the neutral region). In addition, we may have edge leakage current due to a high electric field at the metal-contact periphery or interface current due to traps at the metal-semiconductor interface.

For common high-mobility semiconductors the transport can be adequately described by this thermionic-emission theory. Consider also the diffusion theory
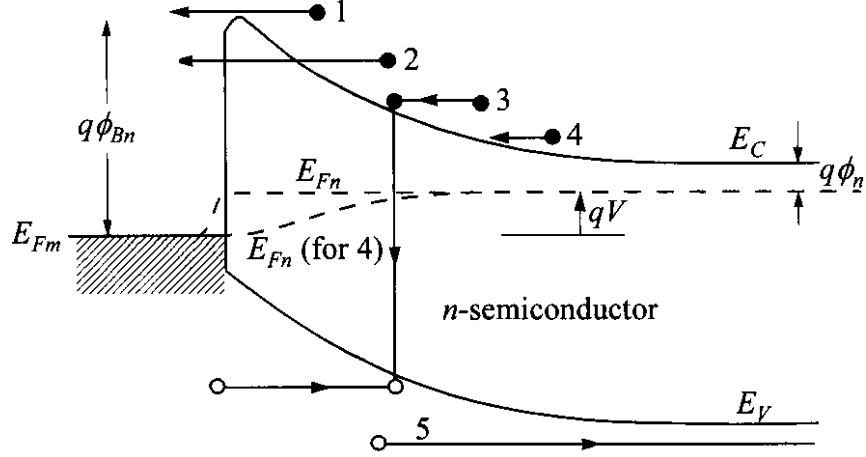
Figure 2.9: Five basic transport processes under forward bias. (1) Thermionic emission. (2) Tunneling. (3) Recombination. (4) Diffusion of electrons. (5) Diffusion of holes.

applicable to low-mobility semiconductors and a generalized thermionic-emission-diffusion theory that is a synthesis of the preceding two theories.

Schottky diode behavior is to some extent electrically similar to a one-sided abrupt $p-n$ junction, and yet the Schottky diode can be operated as a majority-carrier device with inherent fast response. Thus, the terminal functions of a $p-n$ junction diode can general be performed by a Schottky diode with one exception as a charge-storage diode. This is because the charge-storage time in a majority-carrier device is extremely small. Another difference is the larger current density in a Schottky diode due to the smaller built-in potential as well as the nature of thermionic emission compared to diffusion. This results in a much smaller forward voltage drop. By the same token, the disadvantage is the larger reverse current in the Schottky diode and a lower breakdown voltage.

Thermionic-Emission Theory

The thermionic-emission theory is derived from the assumptions that (1) the barrier height $q\phi_{Bn}$ is much larger than kT, (2) thermal equilibrium is established at the plane that determines emission, and (3) the existence of a net current flow does not affect this equilibrium so that one can superimpose two current fluxes - one from metal to semiconductor, the other from semiconductor to metal, each with a different quasi Fermi level. If thermionic emission is the limiting mechanism, then E_{Fn} is flat throughout the deletion region (Figure 2.9). Because of these assumptions, the shape of the barrier profile is immaterial and the current flow depends solely on the barrier is then given by height. The current density from the semiconductor to the metal $J_{s\to m}$ is then given by the concentration of electrons with energies sufficient to overcome the potential barrier and traversing in the x-direction:

$$J_{s\to m} = \int_{E_{Fn}+q\phi_{Bn}}^{\infty} qv_x dn \qquad (2.92)$$

24

where $E_{Fn} + q\phi_{Bn}$ is the minimum energy required for thermionic emission into the metal, and v_x is the carrier velocity in the direction of transport. The electron density in an incremental energy range is given by

$$dn = N(E)F(E)dE \approx \frac{4\pi(2m^*)^{3/2}}{h^3}\sqrt{E - E_C}\exp\left(-\frac{E - E_C + q\phi_n}{kT}\right)dE \quad (2.93)$$

where $N(E)$ and $F(E)$ are the density of states and the distribution function, respectively.

If we postulate that all the energy of electrons in the conduction band is kinetic energy, then

$$E - E_C = \frac{1}{2}m^*v^2 \quad (2.94)$$

$$dE = m^*vdv \quad (2.95)$$

$$\sqrt{E - E_C} = v\sqrt{\frac{m^*}{2}} \quad (2.96)$$

then

$$dn \approx 2\left(\frac{m^*}{h}\right)^3\exp\left(-\frac{m^*v^2}{2kT}\right)(4\pi v^2 dv) \quad (2.97)$$

Equation (2.97) gives the number of electrons per unit volume that have velocities between v and $v+dv$, distributed over all directions. If the velocity is resolved into its components along the axes with the x-axis parallel to the transport direction, we have

$$v^2 = v_x^2 + v_y^2 + v_z^2 \quad (2.98)$$

With the transformation $4\pi v^2 dv = dv_x dv_y dv_z$, we obtain

$$\begin{aligned}
J_{s\to m} =& 2q\left(\frac{m^*}{h}\right)^3\exp\left(-\frac{q\phi_n}{kT}\right)\int_{v_{0x}}^{\infty} v_x\exp\left(-\frac{m^*v_x^2}{2kT}\right)dv_x \\
& \int_{-\infty}^{\infty}\exp\left(-\frac{m^*v_y^2}{2kT}\right)dv_y\int_{-\infty}^{\infty}\exp\left(-\frac{m^*v_z^2}{2kT}\right)dv_z \\
=& \left(\frac{4\pi qm^*k^2}{h^3}\right)T^2\exp\left(-\frac{q\phi_n}{kT}\right)\exp\left(-\frac{m^*v_{0x}^2}{2kT}\right)
\end{aligned} \quad (2.99)$$

The velocity v_{0x} is the minimum velocity required in the x-direction to surmount the barrier and is given by

$$\frac{1}{2}m^*v_{0x}^2 = q(\Psi_{bi} - V) \quad (2.100)$$

Substituting equation (2.100) into equation (2.99) yields

$$\begin{aligned}
J_{s\to m} =& \left(\frac{4\pi qm^*k^2}{h^3}\right)T^2\exp\left(-\frac{q\phi_{Bn}}{kT}\right)\exp\left(-\frac{qV}{kT}\right) \\
=& A^*T^2\exp\left(-\frac{q\phi_{Bn}}{kT}\right)\exp\left(-\frac{qV}{kT}\right)
\end{aligned} \quad (2.101)$$

and

$$A^* = \frac{4\pi q m^* k^2}{h^3} \qquad (2.102)$$

is the effective Richardson constant for thermionic emission, neglecting the effects of optical-phonon scattering and quantum mechanical reflection. For free electrons ($m* = m_0$) the Richardson constant A is 120 A/cm²-K². For multiple-valley semiconductors the appropriate Richardson constant associated with a single energy minimum is given by

$$\frac{A^*}{A} = \frac{1}{m_0}\sqrt{l_1^2 m_y^* m_z^* + l_2^2 m_z^* m_x^* + l_3^2 m_x^* m_y^*} \qquad (2.103)$$

where l_1, l_2 and l_3 are the direction cosines of the normal to the emitting plane relative to the principal axes of the ellipsoid, and m_x^*, m_y^* and m_z^* are the components of the effective mass tensor.

Since the barrier height for electrons moving from the metal into the semiconductor remains the same under bias, the current flowing into the semiconductor is thus unaffected by the applied voltage. It must therefore be equal to the current flowing from the semiconductor into the metal when thermal equilibrium prevails (i.e., when $V = 0$). This corresponding current density is obtained from equation (2.101) by setting $V = 0$,

$$J_{m\to s} = -A^* T^2 \exp\left(-\frac{q\phi_{Bn}}{kT}\right) \qquad (2.104)$$

The total current density is given by the sum of equations (2.101) and (2.104).

$$\begin{aligned}
J_n &= \left[A^* T^2 \exp\left(-\frac{q\phi_{Bn}}{kT}\right)\right]\left[\exp\left(\frac{qV}{kT}\right) - 1\right] \\
&= J_{TE}\left[\exp\left(\frac{qV}{kT}\right) - 1\right]
\end{aligned} \qquad (2.105)$$

where

$$J_{TE} \equiv A^* T^2 \exp\left(-\frac{q\phi_{Bn}}{kT}\right) \qquad (2.106)$$

Equation (2.105) is similar to the transport equation for $p-n$ junctions. However, the expressions for the saturation current densities are quite different.

Diffusion Theory

The diffusion theory is derived from the assumptions that (1) the barrier height is much larger than kT, (2) the effect of electron collisions within the depletion region (i.e. diffusion), is included, (3) the carrier concentrations at $x = 0$ and $x = W$, are unaffected by the current flow (i.e. they have their equilibrium values), and (4) the impurity concentration of the semiconductor is nondegenerate.

Since the current in the depletion region depends on the local field and the concentration gradient, we use the current density equation

$$J_x = J_n = q\left(n\mu_n \mathcal{E} + D_n \frac{dn}{dx}\right) = qD_n\left(\frac{n}{kT}\frac{dE_C}{dx} + \frac{dn}{dx}\right) \qquad (2.107)$$

Under the steady-state condition, the current density is independent of x, and equation (2.107) can be integrated using $exp[E_c(x)/kT]$ as an integrating factor. We then have

$$J_n \int_0^{W_D} \exp\left[\frac{E_C(x)}{kT}\right] dx = qD_n \left\{ n(x) \exp\left[\frac{E_C(x)}{kT}\right] \right\} \Bigg|_0^{W_D} \tag{2.108}$$

and the boundary conditions using $E_{Fm} = 0$ as the reference

$$E_C(0) = q\phi_{Bn} \tag{2.109}$$

$$E_C(W_D) = q(\phi_n + V) \tag{2.110}$$

$$n(0) = N_C \exp\left[-\frac{E_C(0) - E_{Fn}(0)}{kT}\right] = N_c \exp\left(-\frac{q\phi_{Bn}}{kT}\right) \tag{2.111}$$

$$n(W_D) = N_D = N_C \exp\left(-\frac{n\phi_n}{kT}\right) \tag{2.112}$$

Substituting equations (2.109), (2.110), (2.111), (2.112) into equation (2.108) yields

$$J_n = qN_cD_n \left[\exp\left(\frac{qV}{kT}\right) - 1\right] \Bigg/ \int_0^{W_D} \exp\left[\frac{E_C(x)}{kT}\right] dx \tag{2.113}$$

Thermionic-Emission-Diffusion Theory

This approach is derived from the boundary condition of a thermionic recombination velocity v_R near the metal-semiconductor interface. Since the diffusion of carriers is strongly affected by the potential configuration in the region through which the diffusion occurs, consider the electron potential energy versus distance incorporating the Schottky lowering effect as shown in Figure *2.10*. Consider the case where the barrier height is large enough that the charge density between the metal surface and $x = W_D$ is essentially that of the ionized donors. As drawn, the applied voltage V between the
    metal and the semiconductor bulk would give rise to a flow of electrons toward the metal. The electron quasi-Fermi level E_{Fn} in the barrier is also shown schematically as a function of distance. Throughout the region between x_m and W_D

$$J = n\mu_n \frac{dE_{Fn}}{dx} \tag{2.114}$$

where the electron density at any point x is given by

$$n = N_C \exp\left(-\frac{E_C - E_{Fn}}{kT}\right) \tag{2.115}$$

Let us assume that the region between x_m and W_D is isothermal and that the electron temperature T is equal to the lattice temperature.
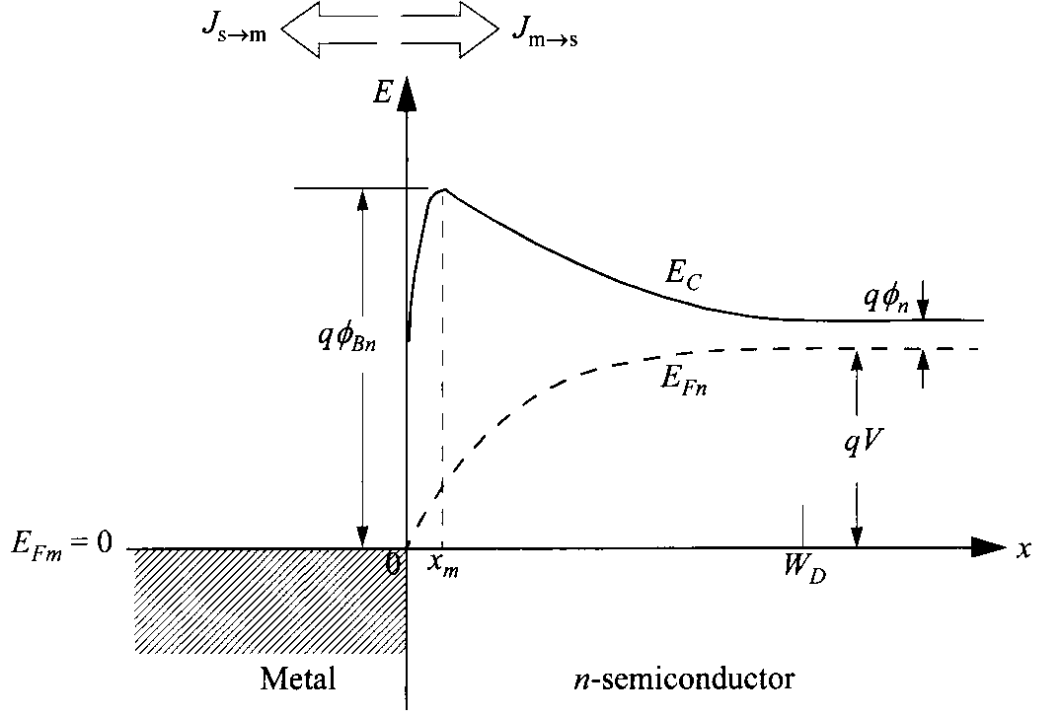
Figure 2.10: Energy-band diagram incorporating the Schottky effect to show the derivations of thermionic-emission-diffusion theory and tunneling current.

If the portion of the barrier between x_m and the interface ($x = 0$) acts as a sink for electrons, we can describe the current flow in terms of an effective recombination velocity v_R at the potential energy maximum x_m:

$$J = q(n_m - n_0)v_R \tag{2.116}$$

where n_m is the electron density at x_m, when the current is flowing,

$$n_m = N_C \exp\left[\frac{E_{Fn}(x_m) - E_C(x_m)}{kT}\right] = N_C \exp\left[\frac{E_{Fn}(x_m) - q\phi_{Bn}}{kT}\right] \tag{2.117}$$

n_0 is a quasi-equilibrium electron density at x_m, the density that would occur if it were possible to reach equilibrium without altering the magnitude or position of the potential energy maximum ($E_{Fn}(x_m) = E_{Fm}$)

$$n_0 = N_C \exp\left(-\frac{q\phi_{Bn}}{kT}\right) \tag{2.118}$$

Another boundary condition, taking $E_{Fm} = 0$ as reference, is

$$E_{Fn}(W_D) = qV \tag{2.119}$$

If n is eliminated from equations (2.114) and (2.115) and the resulting expression for E_{Fn} is integrated between x_m and W_D

$$\exp\left[\frac{E_{Fn}(x_m)}{kT}\right] - \exp\left(\frac{qV}{kT}\right) = -\frac{J}{\mu_n N_C kT}\int_{x_m}^{W_D}\exp\left(\frac{E_C}{kT}\right)dx \tag{2.120}$$

28

Then from equations (2.116) and (2.120), $E_{Fn}(x_m)$ can be solved as

$$\exp\left[\frac{E_{Fn}(x_m)}{kT}\right] = \frac{\upsilon_D \exp(qV/kT) + \upsilon_R}{\upsilon_D + \upsilon_R} \tag{2.121}$$

where

$$\upsilon_D = D_n \exp\left(\frac{q\phi_{Bn}}{kT}\right) \Big/ \int_{x_m}^{W_D} \exp\left(\frac{E_C}{kT}\right) dx \tag{2.122}$$

is an effective diffusion velocity associated with the transport of electrons from the edge of the depletion layer W_D to the potential energy maximum x_m. Substituting equation (2.121) into (2.116) gives the end result of the thermionic-emission-diffusion theory

$$J_{TED} = \frac{qN_C\upsilon_R}{1 + (\upsilon_R/\upsilon_D)} \exp\left(-\frac{q\phi_{Bn}}{kT}\right) \left[\exp\left(\frac{qV}{kT}\right) - 1\right] \tag{2.123}$$

In this equation, the relative values of υ_R and υ_D determines the relative contribution of thermionic emission versus diffusion. In summary, equation (2.123) gives a result that is a synthesis of diffusion theory and thermionic-emission theory, and it predicts currents in essential agreement with the thermionic-emission theory.

Tunneling Current

For more heavily doped semiconductors and for operation at low temperatures, the tunneling current may become more significant. In the extreme of an ohmic contact, which is a metal contact on degenerate semiconductor, the tunneling current is the dominant transport process.

The tunneling current from semiconductor to metal $J_{s\to m}$ is proportional to the quantum transmission coefficient (tunneling probability) multiplied by the occupation probability in the semiconductor and the unoccupied probability in the metal, that is

$$J_{s\to m} = \frac{A^{**}T^2}{kT} \int_{E_{Fm}}^{q\phi_{Bn}} F_S T(E)(1 - F_m) dE \tag{2.124}$$

F_s and F_m are the Fermi-Dirac distribution functions for the semiconductor and the metal respectively, and $T(E)$ is the tunneling probability which depends on the width of the barrier at a particular energy. A similar expression can be given for the current $J_{m\to s}$, which traverses in the opposite direction. In that case F_s and F_m would be interchanged in using the same equation. The total current density, which consists of both thermionic emission and tunneling, can be conveniently expressed as

$$J = J_0 \left[\exp\left(\frac{qV}{\eta kT}\right) - 1\right] \tag{2.125}$$

where J_0 is the saturation current density obtained by extrapolating the current density from the log-linear plot to $V = 0$ and η is the ideality factor, related to

the slope. With little or no tunneling current or depletion-layer recombination, J_0 is determined by that of thermionic emission and η is close to unity. For higher doping and lower temperature, tunneling starts to occur and both J_0 and η increase.

The tunneling current can be expressed analytically and will give more physical insight. This formulation is also used to derive the ohmic contact resistance. Referring to the energy-band diagrams in Figure *2.11*, we can roughly categorize the components into three types: (1) thermionic emission (TE) over the barrier, (2) field emission (FE) near the Fermi level, and (3) thermionic-field emission (TFE) at an energy between TE and FE. While FE is a pure tunneling process, TFE is tunneling of thermally excited carriers which see a thinner barrier than FE. The relative contributions of these components depend on both temperature and doping level. A rough criterion can be set by comparing the thermal energy kT to E_{00}, which is defined as

$$E_{00} = \frac{q\hbar}{2} \sqrt{\frac{N}{m^* \varepsilon_S}} \tag{2.126}$$

When $kT \gg E_{00}$, TE dominates and the original Schottky-barrier behavior prevails without tunneling. When $kT \ll E_{00}$, FE (or tunneling) dominates. When $kT = E_{00}$, TFE is the main mechanism which is a combination of TE and FE.
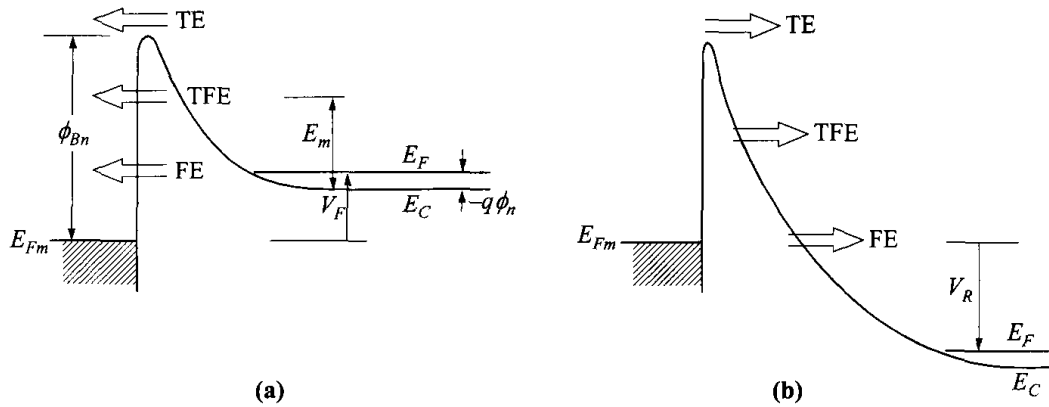
Figure 2.11: Energy-band diagrams showing qualitatively tunneling currents in a Schottky diode under (a) forward bias and (b) reverse bias. TE = thermionic emission. TFE = thermionic-field emission. FE = field emission.

Under forward bias, the current due to FE can be expressed as

$$J_{FE} \approx \frac{A^{**} T \pi \exp[-q(\phi_{Bn} - V_F)/E_{00}]}{c_1 k \sin(\pi c_1 kT)} \tag{2.127}$$

where

$$c_1 \equiv \frac{1}{2E_{00}} \log \left[\frac{4(\phi_{Bn} - V_F)}{-\phi_n} \right] \tag{2.128}$$

The current due to TFE is given by

$$J_{TFE} = \frac{A^{**}T\sqrt{\pi E_{00}q(\phi_{Bn} - \phi_n - V_F)}}{k\cosh(E_{00}/kT)} \exp\left[\frac{-q\phi_n}{kT} - \frac{q(\phi_{Bn} - \phi_n)}{E_0}\right] \exp\left(\frac{qV_F}{E_0}\right)$$
(2.129)

where

$$e_0 \equiv E_{00} \coth\left(\frac{E_{00}}{kT}\right)$$
(2.130)

Minority-Carrier Injection

The Schottky-barrier diode is mainly a majority-carrier device. The minority-carrier injection ratio γ, which is the ratio of minority-carrier current to total current, is small because the minority-carrier diffusion is much smaller than the majority-carrier thermionic-emission current. However, at sufficiently large forward bias, the drift component of the minority carriers cannot be ignored anymore and the increased drift component will increase the overall injection efficiency. Both drift and diffusion of holes lead to the total current of

$$J_p = q\mu_p p_n \mathcal{E} - qD_p \frac{dp_n}{dx}$$
(2.131)

The increased field is set up by the large majority-carrier thermionic-emission current

$$J_n = q\mu_n N_D \mathcal{E}$$
(2.132)

consider the energy-band diagram shown in Figure *2.12* where x_1 is the boundary of the depletion layer, and x_2 marks the interface between the n-type epitaxial layer and the n^+-substrate. From the junction theory, the minority-carrier density at x_1 is

$$p_n(x_1) = p_{n0} \exp\left(\frac{qV}{kT}\right) = \frac{n_i^2}{N_D} \exp\left(\frac{qV}{kT}\right) \approx \frac{n_i^2}{N_D}\frac{J_n}{J_{n0}}$$
(2.133)

where J_{n0} (satur. current density) and J_n are representations of the thermionic-emission current in the following form:

$$J_n = J_{n0} \exp\left[\left(\frac{qV}{kT}\right) - 1\right]$$
(2.134)

The other boundary condition for $p_n(x_2)$ is also necessary to calculate the diffusion current. We use the term transport velocity S_p (or surface recombination velocity) for the minority carriers to relate the current and concentration by

$$J_p(x_2) = qS_p\left[p_n(x_2) - p_{n0}\right]$$
(2.135)

consider the case with $S_p = \infty$. Under this boundary condition, the diffusion component has a standard form as in a $p - n$ junction. From equations (2.131), (2.132) and (2.133) we obtain the total hole current as (for $L \ll L_p$)

$$J_p = \frac{\mu_p n_i^2 J_n^2}{\mu_n N_D^2 J_{n0}} + \frac{qD_p n_i^2}{N_D L} \exp\left[\left(\frac{qV}{kT}\right) - 1\right]$$
(2.136)

31
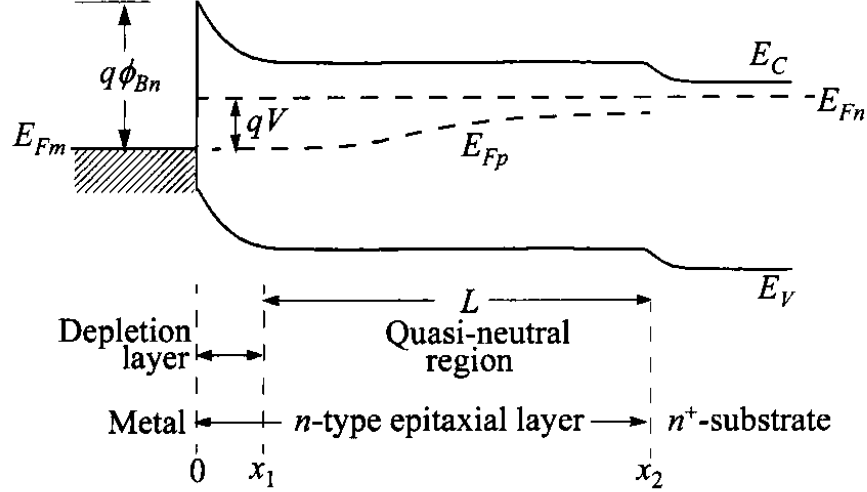
Figure 2.12: Energy-band diagram of an epitaxial Schottky barrier under forward bias.

The injection ratio is given by

$$\gamma = \frac{J_p}{J_p + J_n} \approx \frac{J_p}{J_n} \approx \frac{\mu_p n_i^2 J_n}{\mu_n N_D^2 J_{n0}} + \frac{q D_p n_i^2}{N_D L J_{n0}} \tag{2.137}$$

the injection ratio for low-level bias

$$\gamma_0 = \frac{q D_p n_i^2}{N_D L J_{n0}} \tag{2.138}$$

It is evident that to reduce the minority-carrier injection ratio (to reduce the charge storage time to be discussed below) one must use a metal-semiconductor system with large N_D (corresponding to low resistivity material), large J_{n0} (corresponding to small barrier height), and small n_i (corresponding to large bandgap).

Another quantity associated with the injection ratio is the minority-carrier storage time τ_S, which is defined as the minority carrier stored in the quasi-neutral region per unit current density:

$$\tau_S = \int_{x_1}^{x_2} q p(x) dx / J \tag{2.139}$$

MIS Tunnel Diode

In the metal-insulator-semiconductor (MIS) tunnel diode, a thin interfacial layer such as an oxide is intentionally introduced before metal deposition. This interfacial layer thickness lies in the range of 1-3 nm. This device differs from the MIS capacitor in having appreciable current and under bias the semiconductor is not in equilibrium, i.e. the quasi Fermi levels for electrons E_{Fn} and holes E_{Fp} split. The major differences of this structure compared to a conventional metal-semiconductor contact are: (1) reduced current because of the added interfacial layer, (2) lower barrier height (some potential is developed across the interfacial

layer), and (3) higher ideality factor η. The energy-band diagram is similar to Figure *2.5*. The current equation can be written as

$$J = A^* T^2 \exp(-\sqrt{\zeta}\delta) \exp\left(\frac{-q\phi_B}{kT}\right) \left[\exp\left(\frac{qV}{\eta kT}\right) - 1\right] \qquad (2.140)$$

For the same barrier, the current is suppressed by the tunneling probability $\exp(-\sqrt{\zeta}\delta)$. Here ζ (in eV) and δ (in Å) are the effective barrier and thickness of the interfacial layer. This added tunneling probability can be considered as a modification to the effective Richardson constant. The ideality factor is increased to

$$\eta = 1 + \left(\frac{\delta}{\varepsilon_i}\right) \frac{(\varepsilon_S/W_D) + qD_{its}}{1 + (\delta/\varepsilon_i)qD_{itm}} \qquad (2.141)$$

where D_{its} and D_{itm} are interface traps in equilibrium with the semiconductor and metal. In general, when the oxide thickness is less than 3 nm, the interface traps are in equilibrium with the metal, whereas for thicker oxides, these traps tend to be in equilibrium with the semiconductor. The interfacial layer reduces the majority-carrier thermionic-emission current without affecting the minority-carrier current, which is from diffusion, and raises the minority injection efficiency.

2.3.4 Measurement of Barrier Height

Four methods are used to measure the barrier height of a metal-semiconductor contact: the (1) current-voltage, (2) activation-energy, (3) capacitance-voltage, and (4) photoelectric methods. We focus only on the first method, as it is widely used in this work.

Current-Voltage Measurement

For moderately doped semiconductors, the I-V characteristics in the forward direction with $V > 3kT/q$ is given by

$$J = A^{**} T^2 \exp\left(-\frac{q\phi_{B0}}{kT}\right) \exp\left[\frac{q(\Delta\phi + V)}{kT}\right] \qquad (2.142)$$

Since both A^{**} and $\Delta\phi$ (image-force lowering) are weak functions of the applied voltage, the forward $J - V$ characteristic (for $V > 3kT/q$) is represented by $J = J_0 \exp(qV/\eta kT)$, as given previously in equation (2.125), where η is the ideality factor:

$$\eta = \frac{q}{kT} \frac{dV}{d(\ln J)} = \left[1 + \frac{d\Delta\phi}{dV} + \frac{kT}{q} \frac{d(\ln A^{**})}{dV}\right]^{-1} \qquad (2.143)$$

the barrier height can be obtained from the equation

$$\phi_{Bn} = \frac{kT}{q} \ln\left(\frac{A^{**} T^2}{J_0}\right) \qquad (2.144)$$

In the reverse direction, the dominant voltage dependence is due mainly to the Schottky-barrier lowering (for $V > 3kT/q$)

$$J_R \approx J_0 \approx A^{**}T^2 \exp\left[-\frac{q(\phi_{B0} - \sqrt{q\mathcal{E}_{\updownarrow}/4\pi\varepsilon_s}}{kT}\right] \tag{2.145}$$

where

$$\mathcal{E}_{\updownarrow} = \sqrt{\frac{2qN_D}{\varepsilon_S}\left(V_R + \psi_{bi} - \frac{kT}{q}\right)} \tag{2.146}$$

If the barrier height $q\phi_{Bn}$ is sufficiently smaller than the bandgap so that the depletion-layer generation-recombination current is small in comparison with the Schottky emission current, then the reverse current will increase gradually with the reverse bias as given by equation (2.146), due mainly to image-force lowering.

2.3.5 Ohmic Contact

An ohmic contact is defined as a metal-semiconductor contact that has a negligible junction resistance relative to the total resistance of the semiconductor device. A satisfactory ohmic contact should not significantly perturb the device performance and can supply the required current with a voltage drop that is sufficiently small compared with the drop across the active region of the device.

Specific contact resistance is defined as the reciprocal of the derivative of the current density with respect to the voltage across the interface. When evaluated at zero bias, this specific contact resistance R_C is an important figure-of-merit for ohmic contacts:

$$R_C = \left(\frac{dJ}{dV}\right)^{-1}_{V=0} \tag{2.147}$$

For low to moderate doping levels and moderately high temperatures, $kT \gg E_{00}$, the standard thermionic-emission expression is used to obtain

$$R_C = \frac{k}{A^{**}Tq}\exp\left(\frac{q\phi_{Bn}}{kT}\right) \propto \exp\left(\frac{q\phi_{Bn}}{kT}\right) \tag{2.148}$$

Since only small applied voltage is relevant, the voltage dependence of the barrier height can be neglected. Equation (2.148) shows that low barrier height should be used to obtain small R_C. For higher doping level, $kT \approx E_{00}$, TFE dominates and R_C is given by

$$R_C = \frac{k\sqrt{E_{00}}\cosh(E_{00}/kT)}{A^{**}Tq\sqrt{\pi q(\phi_{Bn} - \phi_n)}}\exp\left[\frac{q(\phi_{Bn} - \phi_n)}{E_{00}\coth(E_{00}/kT)} + \frac{q\phi_n}{kT}\right]$$
$$\propto \exp\left[\frac{q\phi_{Bn}}{E_{00}\coth(E_{00}/kT)}\right] \tag{2.149}$$

This type of tunneling occurs at an energy above the conduction band where the product of carrier density and tunneling probability is at a maximum.

With even higher doping level, $kT \ll E_{00}$, FE dominates, and the specific contact resistance is given by

$$R_C = \frac{k \sin(\pi c_1 kT)}{A^{**}\pi qT} \exp\left(\frac{q\phi_{Bn}}{E_{00}}\right) \propto \exp\left(\frac{q\phi_{Bn}}{E_{00}}\right) \qquad (2.150)$$

Provided that the barrier height cannot be made very small, a good ohmic contact should operate in this regime of tunneling.

Specific contact resistance is a function of the barrier height (in all regimes), doping concentration (in TFE and FE), and temperature (more sensitive in TE and TFE). Qualitative dependence on these parameters is shown in Figure *2.13* for a fixed semiconductor material. The trend and the regimes of operation are also indicated in the figure. In TE, R_C is independent of doping concentration and dependent only on the barrier height ϕ_B. In the other extreme of FE, in addition to ϕ_B, R_C has a dependence of $\propto \exp(N^{-1/2})$.
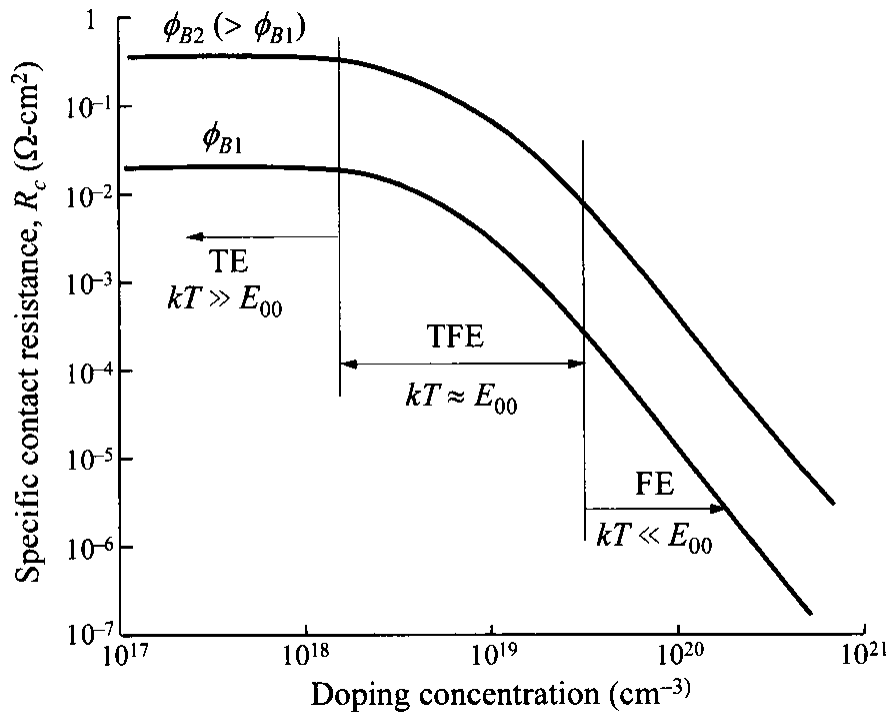
Figure 2.13: Dependence of specific contact resistance on doping concentration (and E_{00}), barrier height, and temperature. Regimes of TE, TFE, and FE are indicated.

3. Experiment

3.1 Samples

3.1.1 Preparation

As a initial material for sample preparation was used a planar monocrystalline wafer of $CsPbBr_3$ perovskite of the thickness of about $2\ mm$. From such form a cut was perfomed to creation of bar-like samples. This was accomplished by a diamond wire saw (Well Diamond Saws Inc., model 6234) using a wire of diameter of $200\ \mu m$, which was cooled by oil during the cutting process. Oil was chosen instead of water with redards to perovskite low durability to this medium. After this step, the bar-shaped sample was polished using abrasive based on Al_2O_3 with maximum size of grains of $0.3\ \mu m$. The process was ensured on the Polytex cloth in WD-40 oil thick layer. The sample bar was then washed in toluene to remove mechanical and chemical residues seated on the sample and came from previous processes. Finally, the sample was dried using air flow.

3.1.2 Contacting

After polishing process, the samples were covered by a polymer tape alongside the bar and the only two heads of the bar remained uncovered. This step masked the sample for implementation the current contacts on opposite sides. For formation of potential probes, slightly different technique was used. By using mechanical mask with appropriate holes, with aspect to their sizes and positions, were created contacts in a row on the longer side of the sample bar. The deposition process itself was performed, in the sealed chamber, by vacuum evaporation from the boat. Materials of $5n$ purity for this step were came by company of Safina, in this case the chromium and gold were used. The chromium for contacts of sample marked as CPB19, and the gold for CPB7 sample. Each with the single type of contacts, definitely. Thereby process, contacts of tens of nanometers thickness were achieved.

Next proceedings contained sticking the sample on a sapphire pad by thermally conductive silicon paste. Then I did the coupling of contacts on the sample with silver wires, with a diameter of $50\ \mu m$, by coloidal graphite conductive aqueous based adhesive (Alfa Aesar, Thermo Fisher Kindel) of resistance of $3\ \Omega/cm^2$ at $250\ \mu m$ thick layer, as shown in Figure *3.1*.

The sapphire pad with the sample bar was placed onto the holder and were performed the soldering of silver wires from sample contacts to pins located on the holder. The holder itself is the part of sample positioner which is formed for insertion into the cryostat (Janis Research). This cryostat is suitable for temperature dependence measurements as well as measurements under the inert gas atmosphere, here using nitrogen of purity class 4.7.

Arrangement of contacts on the sample has two variants - in a row and laterally, as shown in Figure *3.2*. A both variants allow measurements of conductivity, i.e. when current contacts (pins 4 and 5) measure the current only and potential contacts (pins 2 and 1 in Figure *3.2a* or pins 3, 2, 1 in Figure *3.2b*) measure the
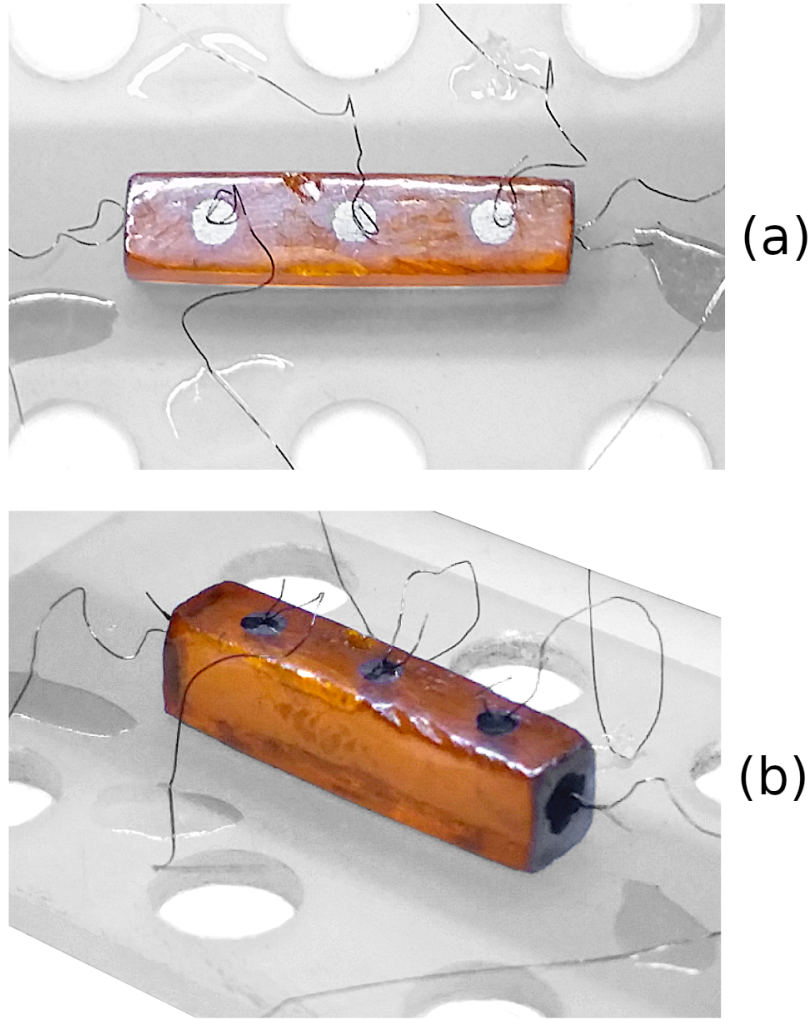
Figure 3.1: CPB7 sample bar: here, still with testing chromium contacts, (a) before steady coupling of contacts with silver wires, (b) after using coloidal graphite adhesive for solid joining.

voltage only. For instance *2-1 5-4* where the first couple of numbers stand for combination for voltage measurement and the second pair is for combination for current measurement. This kind of connection is known as Four Point Method, and is not appointed to characterize properties of the barrier at current contacts. Then again, connection where one of current contacts (pins 4 or 5) or even a both, is measuring current and voltage together, then properties of the barrier, at corresponding current contact, are incorporated, i.e. for instance *5-2 5-4* where the first couple of numbers stand for combination for voltage measurement and the second pair is for combination for current measurement. Such connection is named as Three Point Method. Furthermore, the arrangement of contacts as shown in Figure *3.2a* permits measurement of the Hall effect for recognises a type of semiconductor. Here can be chosen the combination including voltage measurement between pin 2 and 3. Regrettably, it was impossible to acquire reliable data from such measurement due to low signal-to-noise ratio.
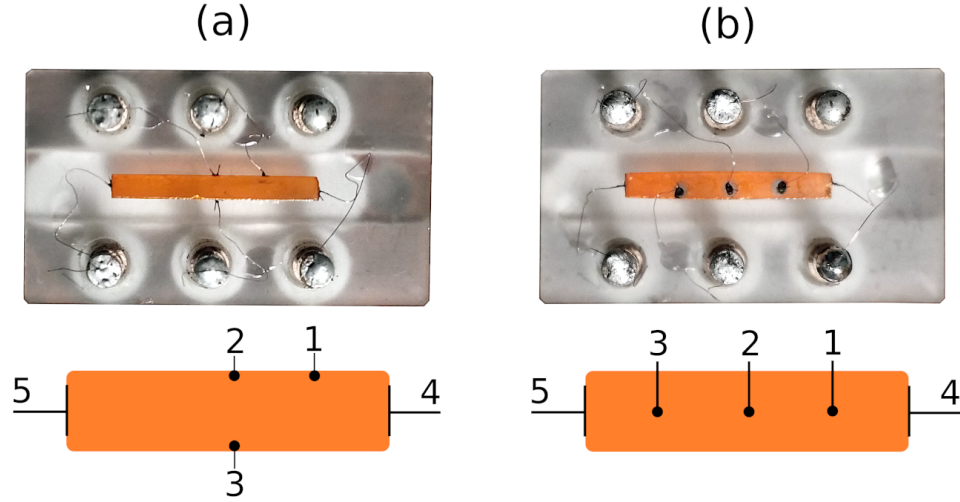
Figure 3.2: Arrangements of contacts of CPB19 samples, (a) laterally located contacts, (b) in a row contacts.

3.1.3 Dimensions

For calculations and resulting determination of transport parameters have precise dimensions and distances, of tested samples, a crucial importance. Values in Table *3.1* are in according to Figure *3.2*. Dimensions of CPB19 samples are (in mm) 1.72 x 1.46 x 12.6 (h x w x l).

Contacts[a]	Distance [mm]	Contacts[b]	Distance [mm]
5–2	6.3	5-3	3.3
2–1	3.0	3-2	3.1
1–4	3.3	2-1	3.2
—	—	1-4	3.0

Note: [a] sample with laterally located contacts, [b] sample with contacts in a row

Table 3.1: CPB19 sample: distances of contacts.

3.2 Measurement Technique

For complete fulfil of the task, the measurement technique of current-voltage characteristics (also I-V characteristics) was chosen. It is relationship between current which we let into the sample and relevant feedback in the form of voltage. In our case, the proper considerations about the amount of electric current were crucial because voltage feedback of the sample often reached the voltage limit which was given by used current source. Derived measurement from I-V characteristics are detection of hysteresis behavior and also measurement evaluation in the time for finding time stability of carrier collection.

3.3 Device Scheme

Measuring setup consists of individual electrical instruments and cryostat part, where the sample has been placed. Detailed scheme is shown in Figure *3.4*. Generally, it includes devices such as source (current, temperature, gas), switching (current), sensors (pressure, temperature) and reading (current, voltage, temperature, pressure).

As a central instrument of the measuring setup was the current source Keithley 220 controlled by computer. It has bipolar voltage limit up to 105 V and ranges (for our purposes) 1 nA, 10 nA and 100 nA, with response time < 3 ms. For guarding measurement was used the Guarded Adapter Keithley 6167 directly connected to the current source instrument. A brief scheme of guarded measurement is shown in Figure *3.3*, where $I_{Meas} = I_{DUT} + I_{Leak} = I_{DUT} + V_{Set}/R_{Leak}$ for Figure *3.3a*, whereas $I_{Guard} \approx 0$ and $I_{Meas} = I_{DUT}$ for Figure *3.3b*. Hereafter subsumed current source Keithley 2450 had guarding option already integrated in the body.
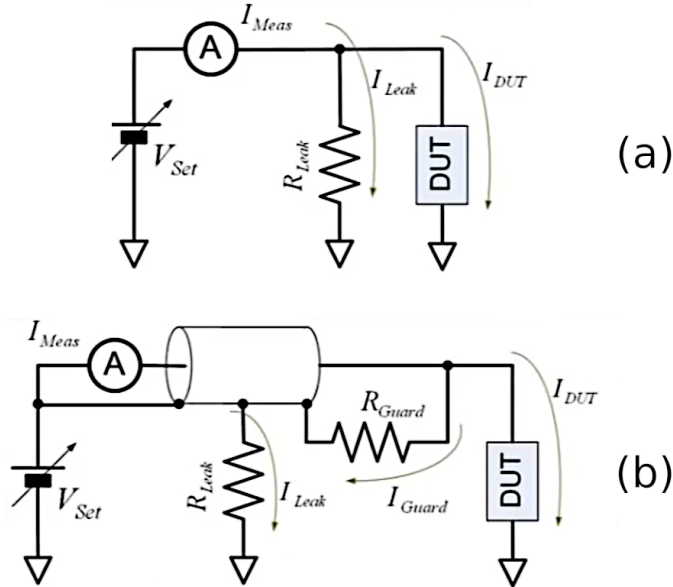
Figure 3.3: Guarding technique: (a) without guarding, (b) with guarding.

The picoammeter Keithley 6485 was subsumed into the system for reading of the actual current values. It has current range from 2 nA to 20 mA, which was a problem due to our measurements commonly performing in the region from 0 nA to 5 nA and beyond. For combinations changing purposes, i.e. for quick and proper reconnection of the current and voltage pins of the sample, was subsumed Switch System Keithley 7001 with the Low Current Matrix Card model 7152 inside. The Low Current Card was chosen for high resistivity measurement ability and for matrix configuration of 4 rows by 5 columns. Voltage reading was ensured by set of two Programmable Electrometers Keithley 6514 with burden voltage correction for minimizing of total voltage offset, connected to Autoranging Multimeter Keithley 2010.

All of mentioned electrical instruments are connected via GPIB interfaces to the PC within the framework of bi-directional communication.
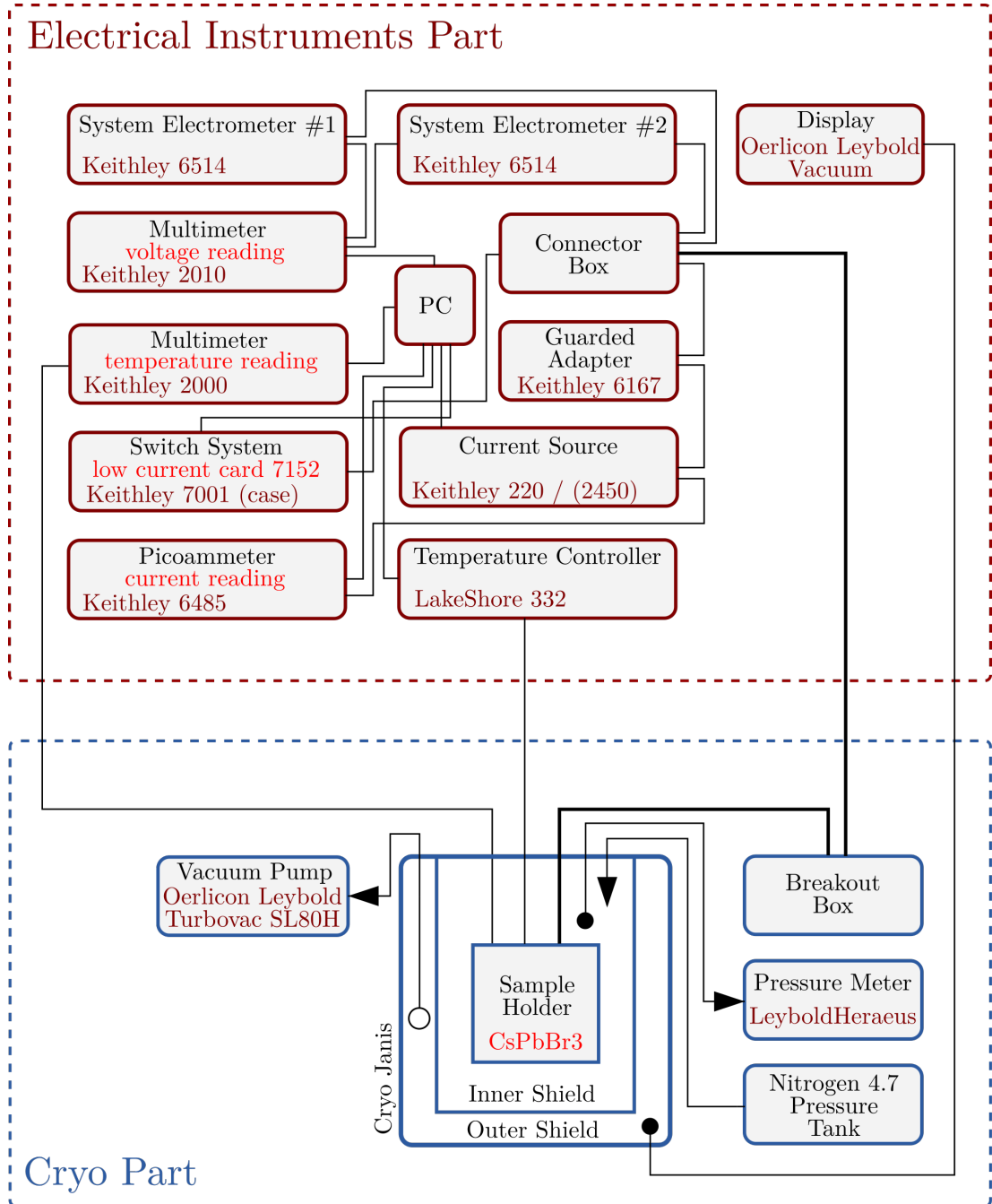
Figure 3.4: Scheme of measuring setup.

4. Results and Discussion

This chapter incorporates a summary of finally selected measurements, their results and analyses. All results have been acquired on two samples - CPB19 and CPB7, as mentioned in the previous chapter. Each of samples was subjected of measuring technique of current-voltage characteristics. Post-processing of retrieved data allows to represent them to two various forms, which tell us not only the development of the bias and the current dependences, but also comprehensive behavior in time evolution.

4.1 Current-Voltage Characteristics

The measurement uses two methods: in group and not in group. The first mentioned approach involves measurements where all measured combinations are measured immediately after each other, so almost at once. They thus have a very small time distance from each other. In contrast, the second method performs measurements by measuring one whole combination at a time and only then proceeding to measure the next combination. Furthermore, it is necessary to mention that all measurements took place under the voltage limit of 100 V, which was given by the current source used, as mentioned in the previous chapter.

By performing several test measurements, I found that it is not possible to perform measurements at a temperature of 300K, due to the rapid reaching of the voltage limit. At the same time, it was necessary to measure at currents whose signal would have a distance from noise. The only option was to increase the temperature by 33K. Therefore, successful measurements are mainly reported at a temperature of 333K. Furthermore, by measuring the current-voltage characteristics, the hysteresis was detected, as shown in Figure *4.1*. Since it was still present in subsequent control measurements, I decided to examine it in more detail, as shown in Figure *4.2* for sample CPB19 with chromium contacts [15] and in Figure *4.3* for sample CPB7 with golden contacts [16], [17]. For both measurements, the entire hysteresis curve was run for four times. The presence of a barrier is evident here, for some voltage, the current rises, and its breakthrough through the tunnel effect. This is a reversible process.

Due to the small current range of these mentioned measurements, I proceeded to extend it up to values in the range of $\pm$ 30 nA. Two such measurements are shown in Figure *4.4* and in Figure *4.5*. These measurements were taken considering how the curve would evolve if I stayed at one value after some steady steps. I did this at values of 10 nA, 20 nA and 30 nA, where I measured ten values each time. However, the curves shown differ considerably, although they are the same measurements, over the same and entire sample. The only difference was the time interval between these measurements. While the *4.4* was taken on 12.4.2023, the *4.5* then on 30.6.2023 Thus, a wild development is noticeable in the sample, which was subjected to additional measurement loads in the time between these measurements.

Nevertheless, I still proceeded to explore the moment in the curve when I require the measuring apparatus to run up to the point where I will measure repeatedly. Therefore, around such a point I set the measurement of ten values

before and ten values after. The results are shown in Figure *4.6* in the voltage expression and in Figure *4.7* in the time expression. Overall, however, it can be seen that due to unremitting changes in the results of the current-voltage characteristics, it is not possible to determine the contact characteristics from them. It is noticeable that the hysteresis changes depending on time and history of the measurement, so I proceeded to preferably measure the time characteristics. Similarly, finding that the hysteresis changes depending on how fast I measure, i.e. the acquisition time of each measured point. It is also important to state that the cause of hysteresis behavior is electromigration or rather ion migration, respectively.
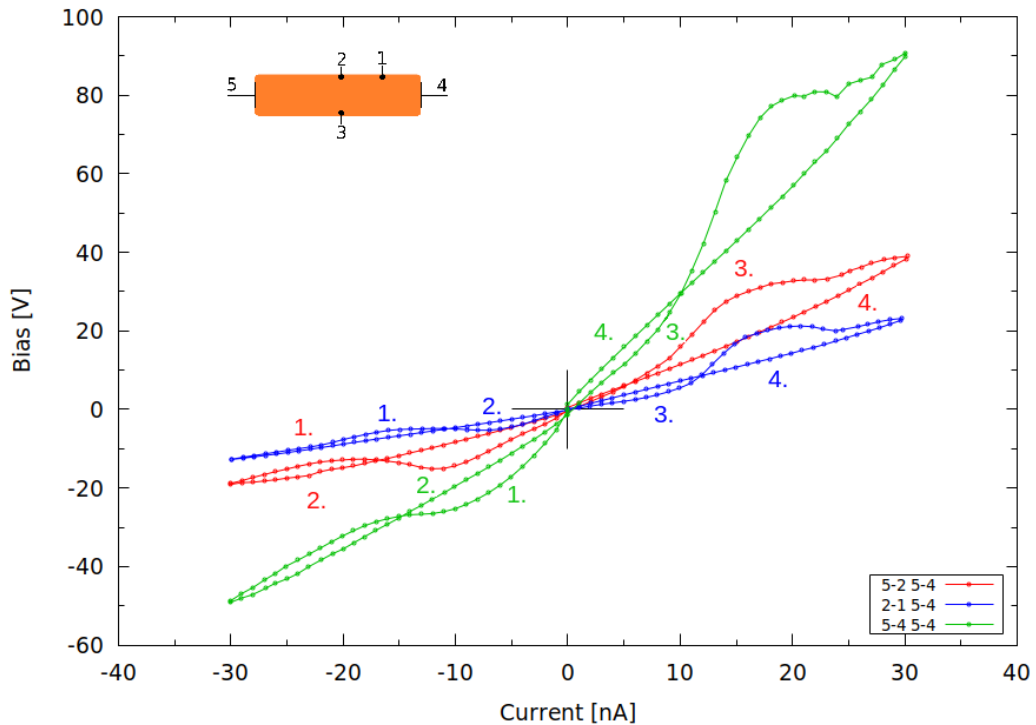
Figure 4.1: I-V characteristics of sample CPB19, measured in group at 333K, chromium contacts, coloured numbers close by curves denotes order of measurements.

In the case of I-V characteristics, we see a binding phenomenon - at low voltages and currents, the resistance increases, at higher currents, on the contrary, the resistance decreases. We are then working on a model explanation of the phenomenon and we are not yet clear about it. We observe these phenomena not only on the entire sample bar, but also on the middle zone between contacts 1 and 2 in Figure *4.1*. Such development is impossible in the ideal four-point method. For the sake of explanation, I consider the carrier depletion model under the dominant contact, that is, the one that supplies the sample with the majority of carriers, in our case apparently holes. Due to the small concentration of carriers and electrically active defects with levels close to the Fermi energy, it can easily lead to a situation where the depletion thickness spreads over the entire sample bar, which would lead to the observed phenomena. However, further experiments will be necessary to confirm the model.
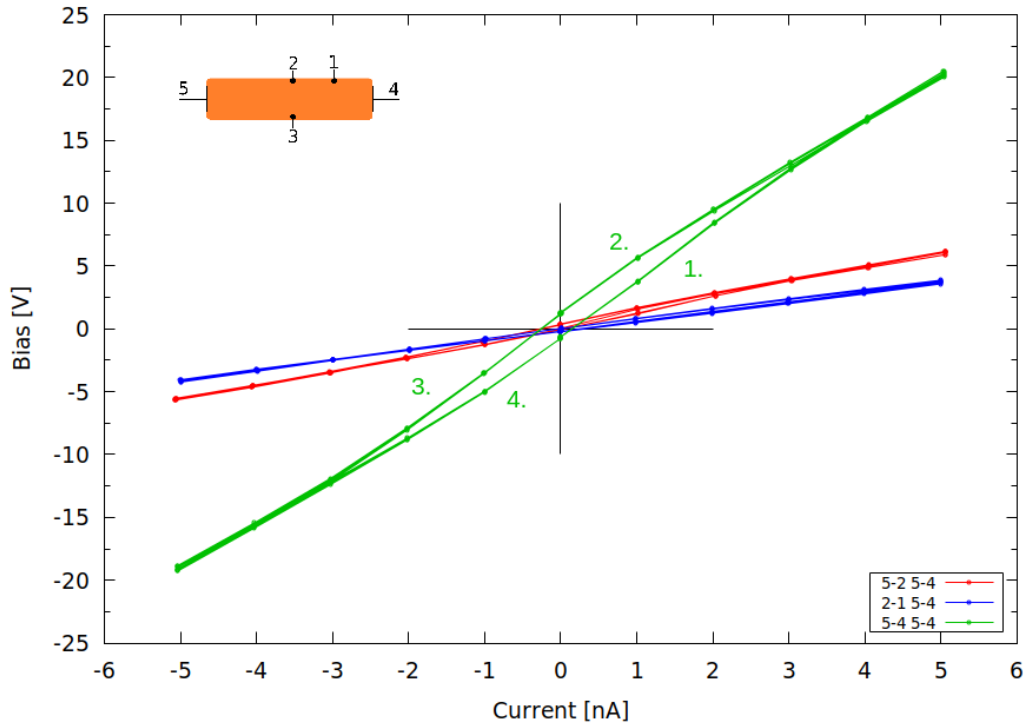
Figure 4.2: I-V characteristics of sample CPB19, measured not in group at 333K, chromium contacts, green numbers close by curves denotes order of measurements.
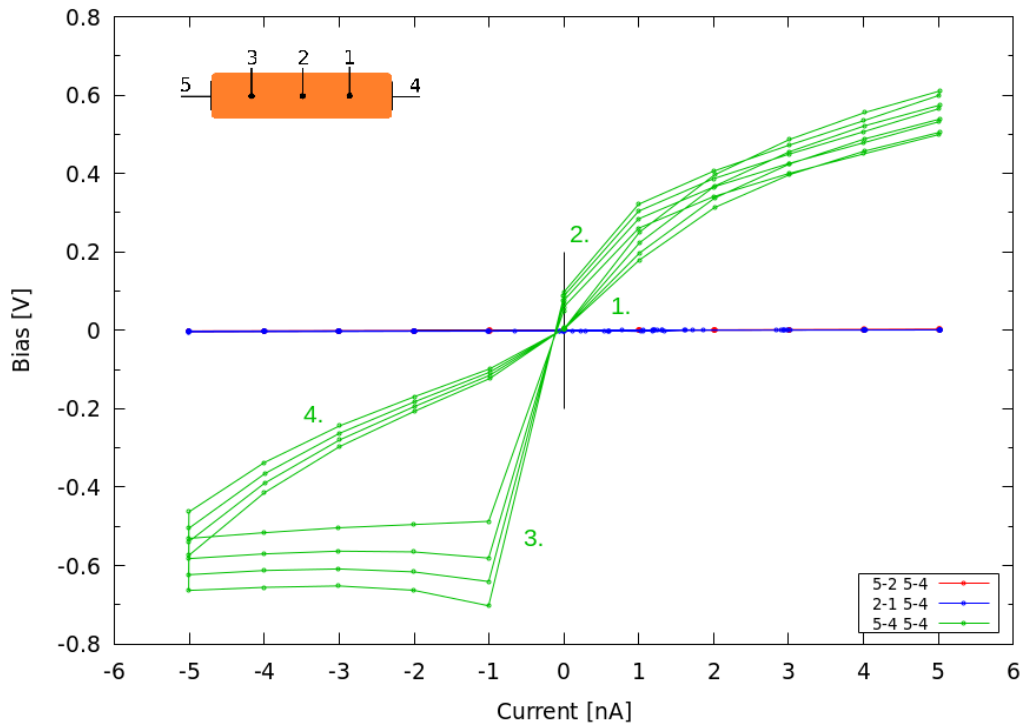
Figure 4.3: I-V characteristics of sample CPB7, measured not in group at 300K, golden contacts, green numbers close by curves denotes order of measurements.
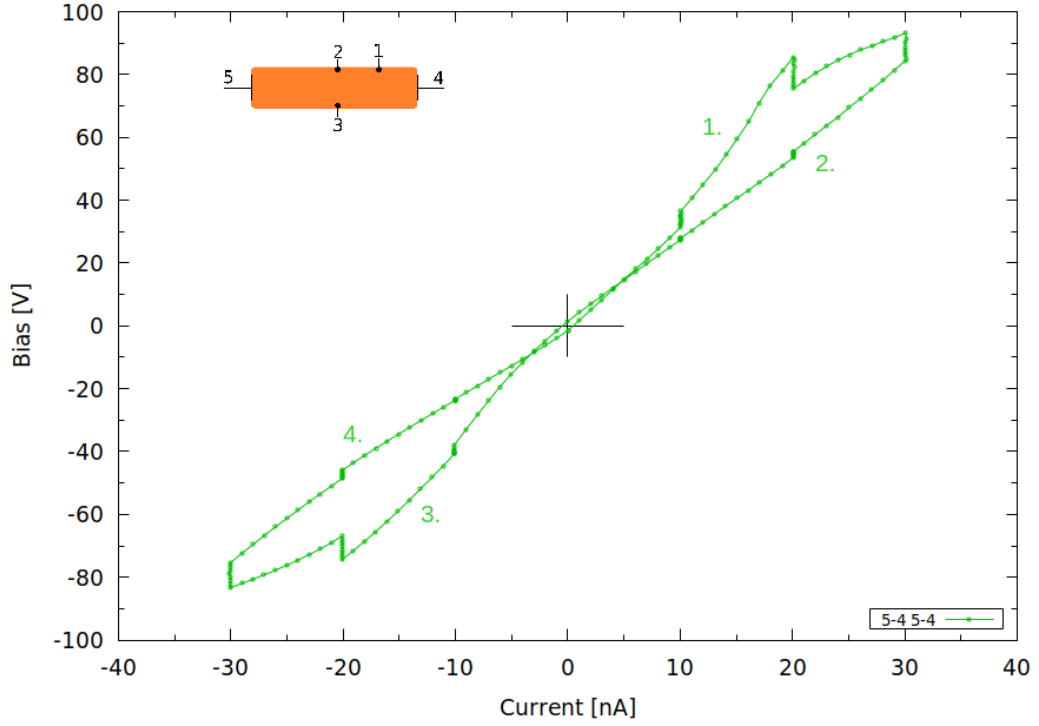
Figure 4.4: I-V characteristics of sample CPB19, measured 12.4.2023 at 333K, chromium contacts, green numbers close by curves denotes order of measurements.
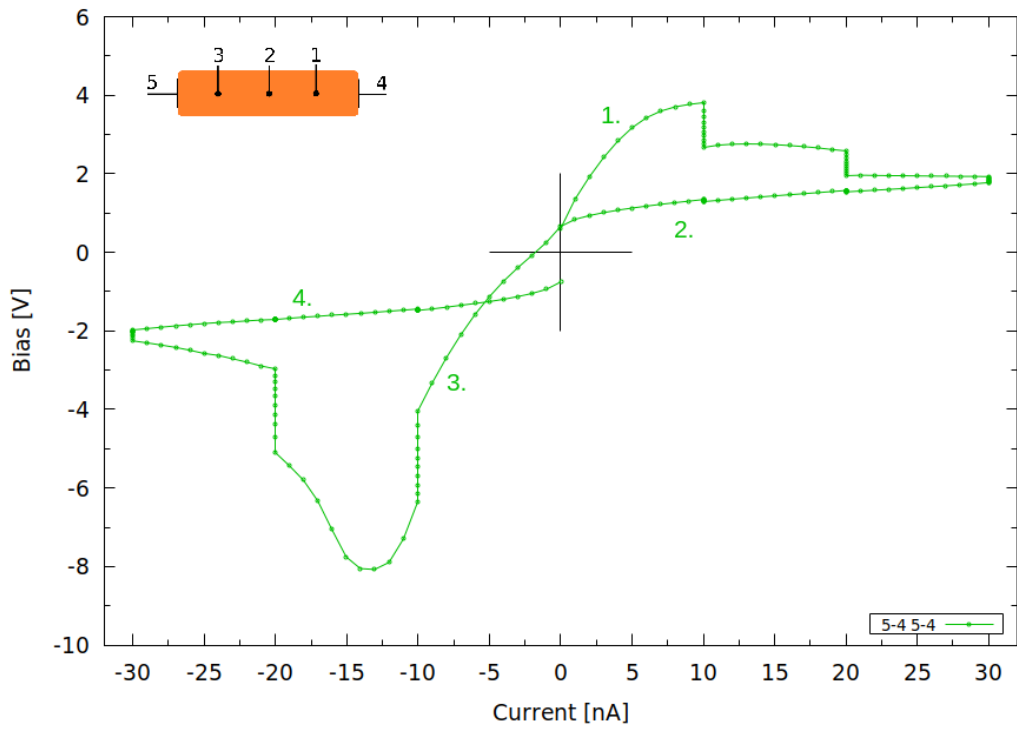
Figure 4.5: I-V characteristics of sample CPB19, measured 30.6.2023 at 333K, chromium contacts, green numbers close by curves denotes order of measurements.
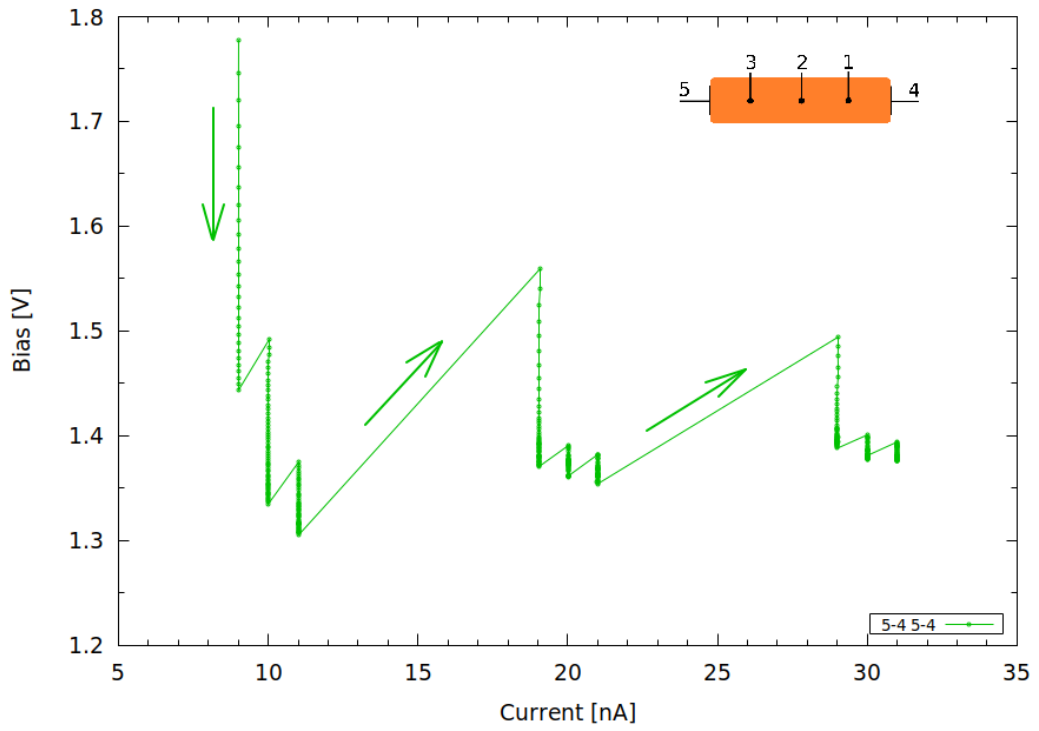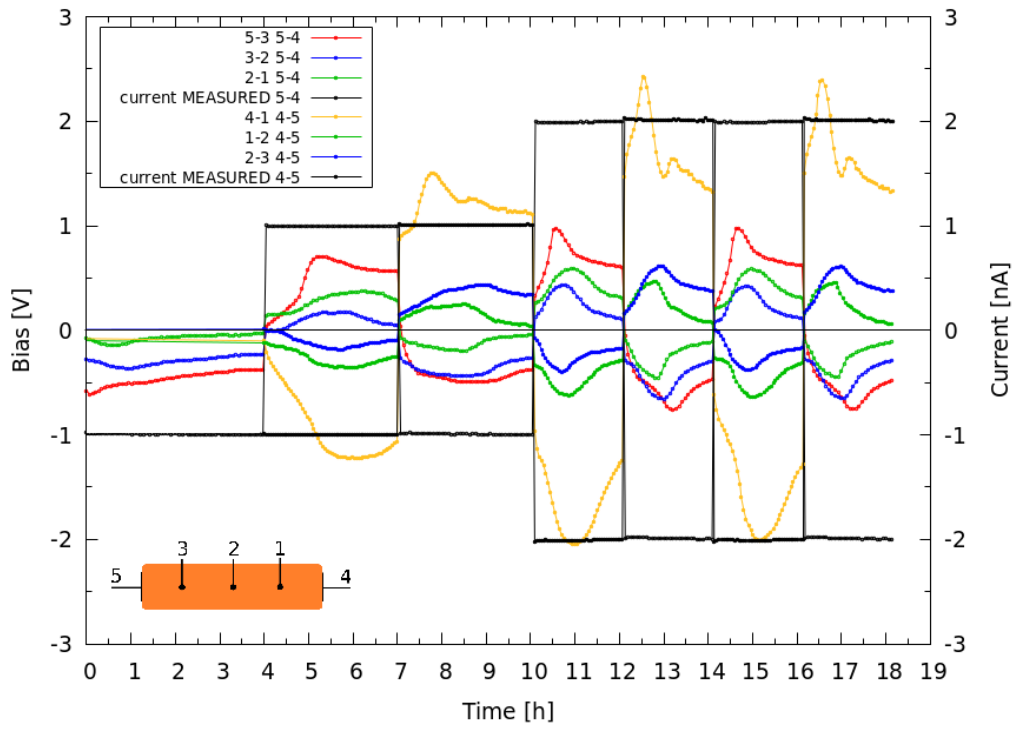
Figure 4.6: I-V characteristics of sample CPB19, measured at 333K, chromium contacts.
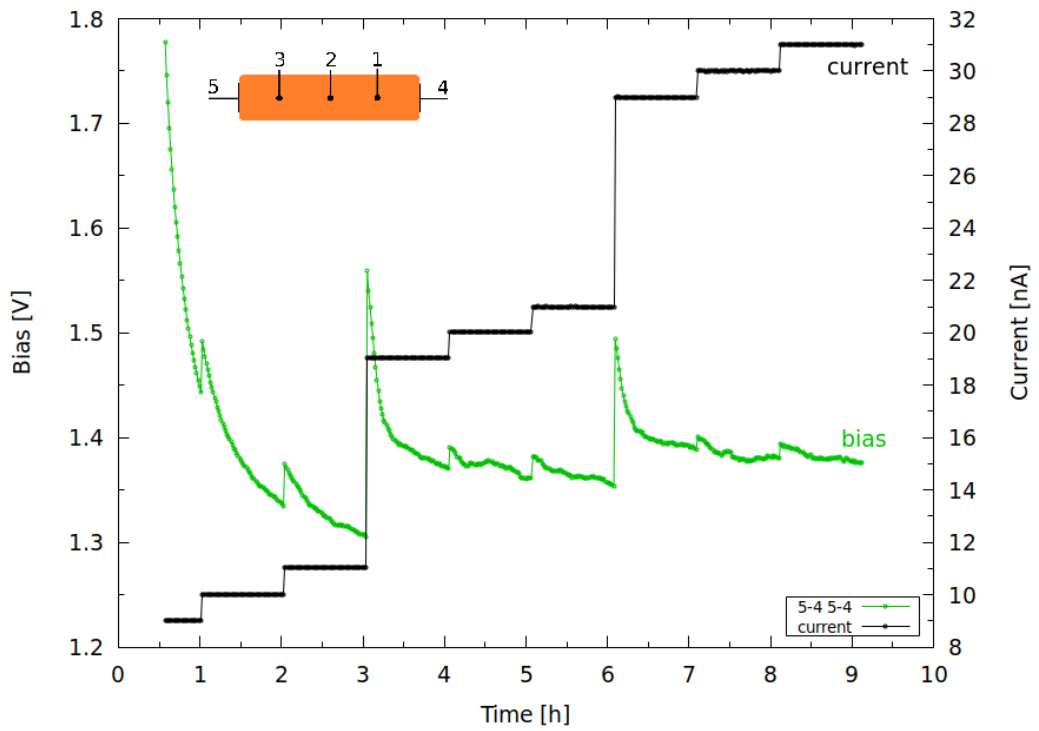
Figure 4.7: U-t-I evolution of sample CPB19, measured at 333K, chromium contacts.

4.2 Time Stability of Carrier Collection

As an initial measurement, I chose a time characteristic with three temperature levels, to see how temperature would affect this kind of experiment. As you can see in Figure *4.8*, the effect is not so convincing, rather in the expression of the resistance, and its slight increase for low temperature is noticeable in Figure *4.9*. So I made a measurement to monitor the behavior over time at variable current values of ± 4 nA and ± 15 nA in Figure *4.10* and Figure *4.11*

The result was, similar to the previous measurement, the presence of the phenomenon of electromigration, or ion migration. So I proceeded to the measurement, which would take place in both directions through the sample, with the observation of the development and the possibility of symmetrical behavior of such an experiment. I set it at two temperatures as shown in Figure *4.12* and in Figure *4.13*. By comparing the results, it can be said that significant differences occur mainly in the direction of the current of combination $4 - 5$. In order to evaluate the transport parameters that I want to obtain, I therefore decided to measure in one direction of the current with a sample in combination $5 - 4$. I processed it in Figure *4.14*, Figure *4.15* and Figure *4.16* for three different temperatures.
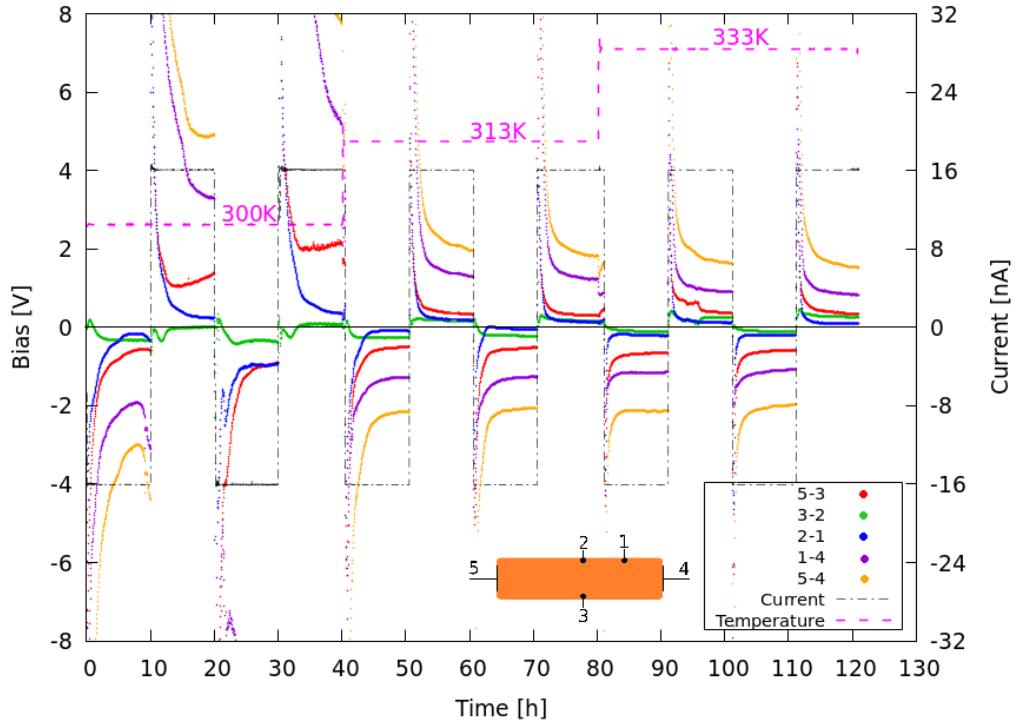
Figure 4.8: Temperature dependence measurement in group, sample CPB19, bias expression, chromium contacts.

We can see advancing waves of resistance growth, moving from anode to cathode. This fact we regard as a fundamental of this thesis. This is a proven electromigration of the defect. These defects are undoubtedly positively charged and
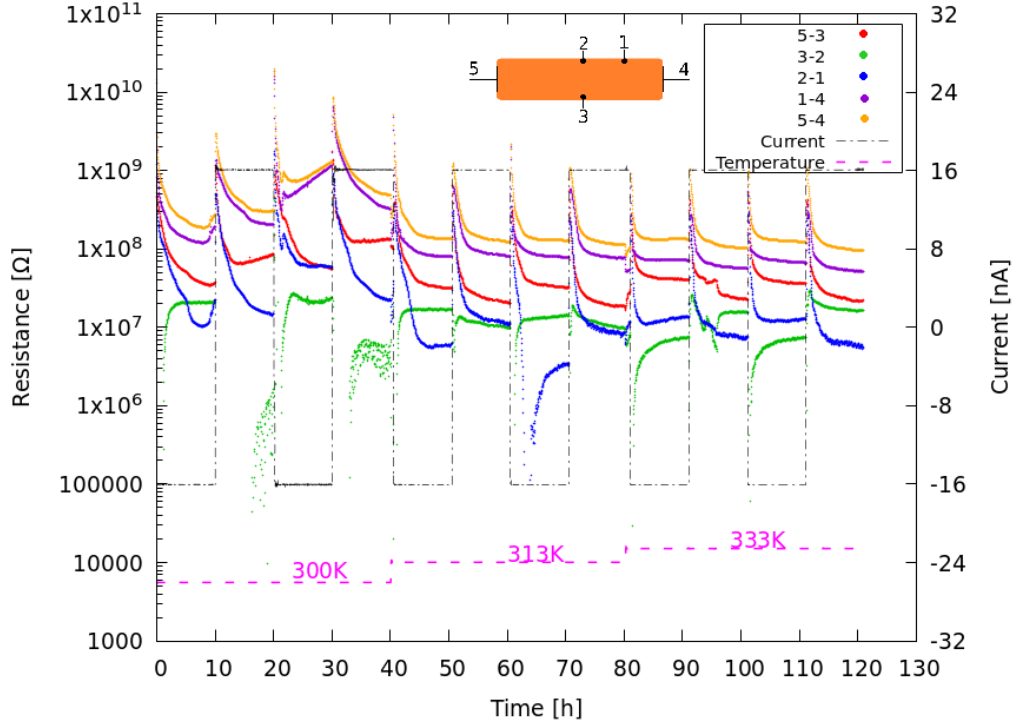
Figure 4.9: Temperature dependence measurement in group, sample CPB19, resistance expression, chromium contacts.

rapidly drift in eletric field by the whole sample bar. At the same time, we prove with these measurements that it is a *p*-type material. This is also a non-trivial result. Finding the type of conductivity in a semiconductor with low electron mobility and holes by measuring the Hall effect can be difficult. Here we see it indirectly, but clearly interpretable.

Due to the speed of diffusion, I suspect that the defects drift along the surface of the sample, where such rapid processes can be expected. The concentration of defects will be low and will not block the electric field inside the sample. Therefore, it is not possible to determine from our measurements whether the defects are on the surface or in the volume.

In measurements, we can see the phenomenon of electromigration at low voltages, when ions drift relatively slowly and we are able to capture their movement between zones. At higher voltages, this process happens quickly and we can see some subsequent relaxation that leads to a decrease in resistance. This phenomenon is common to the measurement of I-V curves at higher currents.
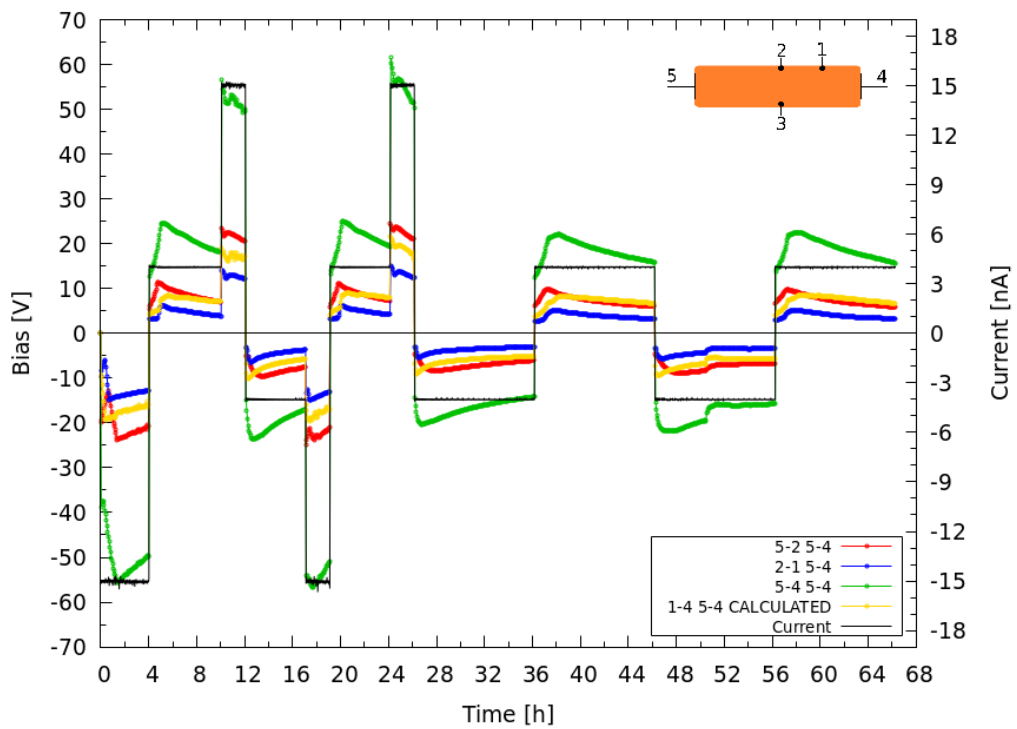
Figure 4.10: Current dependence measurement in group, sample CPB19, bias expression, chromium contacts.
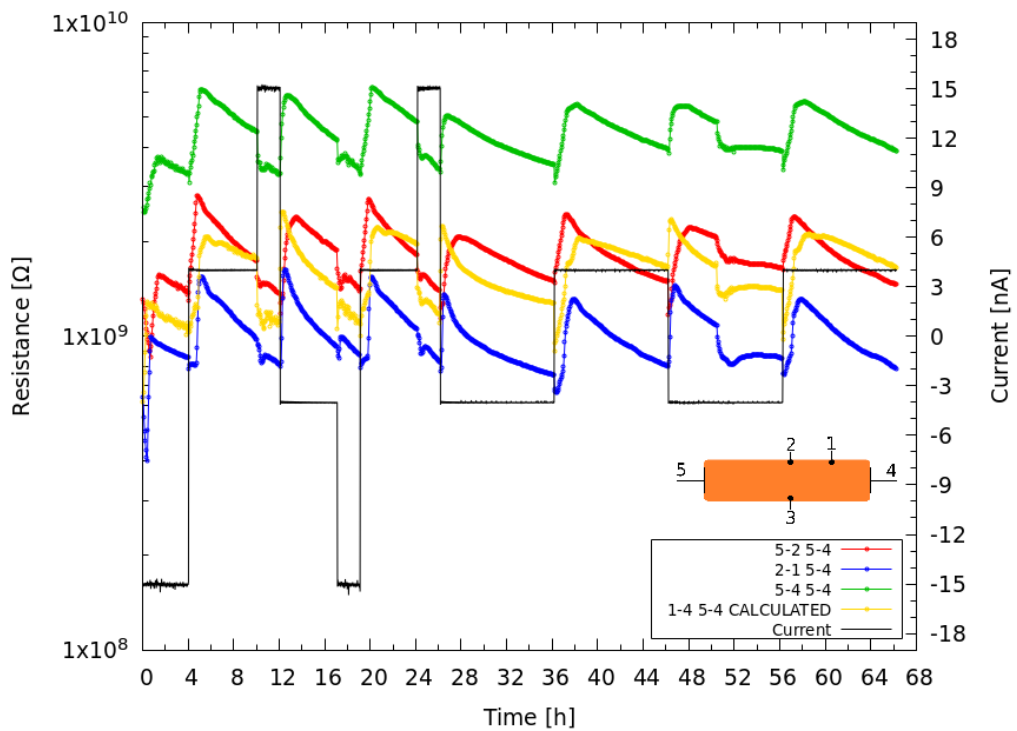
Figure 4.11: Current dependence measurement in group, sample CPB19, resistance expression, chromium contacts.

Figure 4.12: U-t-I evolution of sample CPB19, measured in group at 313K, chromium contacts.
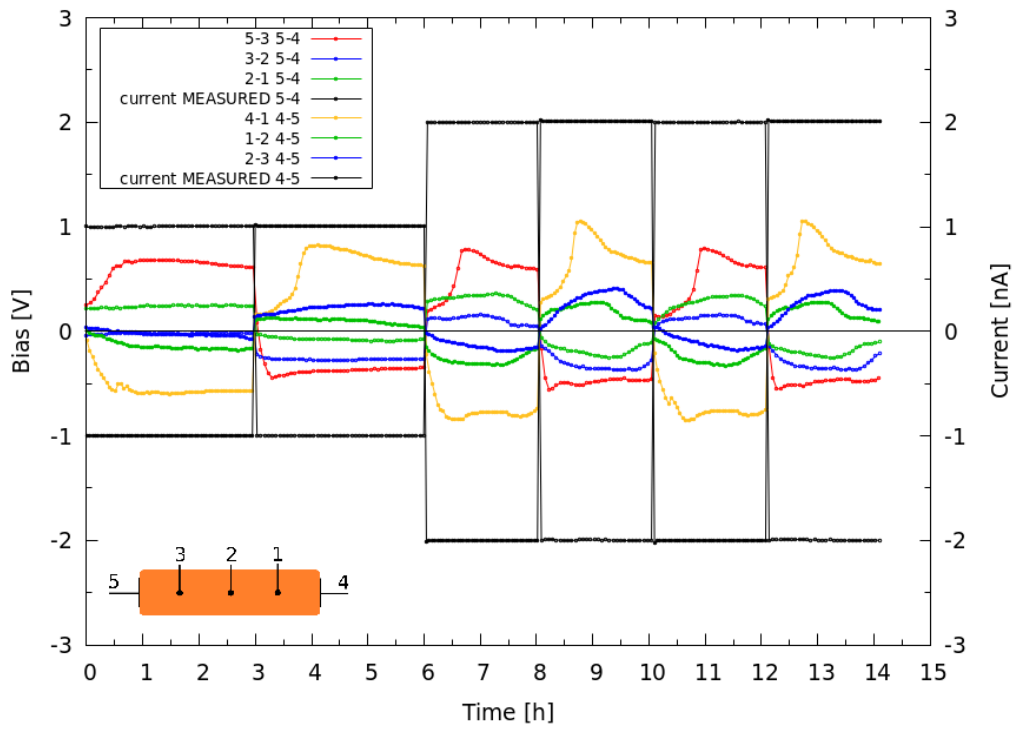
Figure 4.13: U-t-I evolution of sample CPB19, measured in group at 333K, chromium contacts.

4.2.1 Transport Parameters Calculation

Based on the data that are shown in Figures *4.14*, *4.15*, *4.16*, the transport parameters were calculated, always for the last four current intervals. The results are listed in tables below and are within the ranges reached in accordance with [9], [10], [11], [12] and [13], [14].

Relations for calculation of transport parameters are presented in Chapter 2. Specifically, relation (2.11) was used to calculate the electric field and it is the field between the peaks of the respective curves in one interval. The mobility of the ions was given by the relation (2.10), more detailed (2.15), respectively. I obtained the value of the diffusion coefficient from Einstein relation (2.53). In tables below, I present the numbers to one decimal place, as an error in tens of percent is expected.

It can be seen from the results that the temperature dependence of both the mobility and the diffusion constant is non-monotonic in the indicated temperature interval of 300 to 333K. This result is highly suspect due to the narrow temperature range used. From a general point of view, it is unlikely that I would hit directly at the temperature where a change in the transport mechanism occurs, which would lead to the observed development. Therefore, I present the results as preliminary, which will require repeated measurements, including an extended temperature interval, in order to verify that the result is repeated.

However, the observed development is not in principle impossible. There are models that could lead to an observed non-monotonic dependence. Their principle is relatively non-trivial and is related to the defect structure of the perovskite and the chemical reaction between the defects. I originally planned to also find out the effect of temperature on the rate of reactions. However, due to the non-monotonic behavior of mobility, drawing an Arrhenius graph is unnecessary. I will most likely not determine anything from him. [31] One can only expect an energy value with an enormous error from the interpolation, and this error will be larger than the detected value.
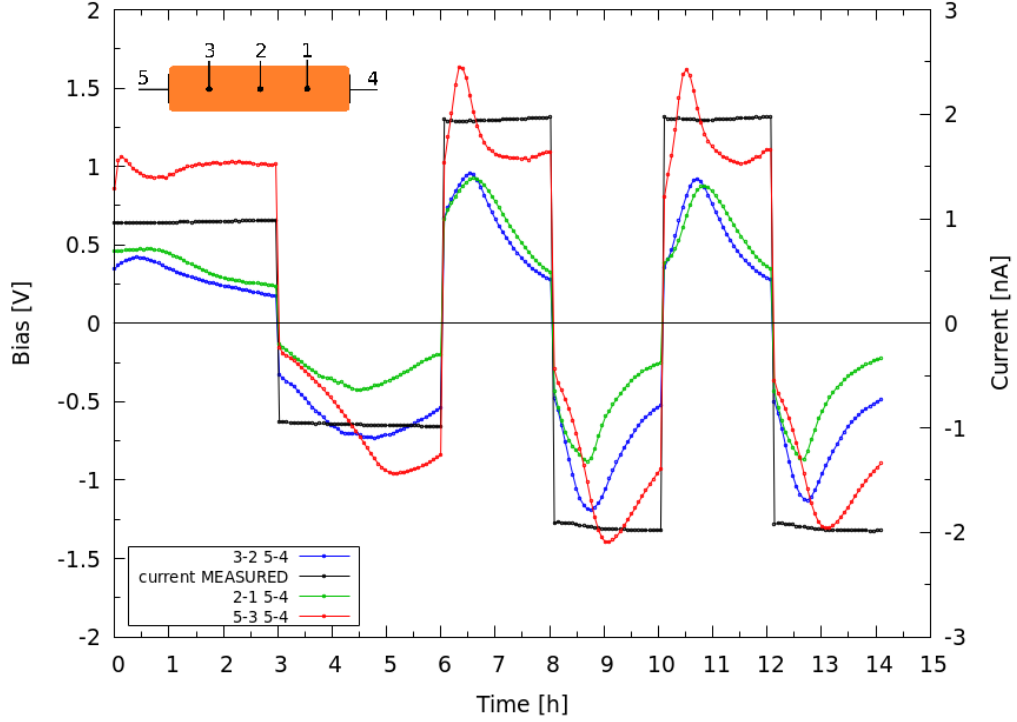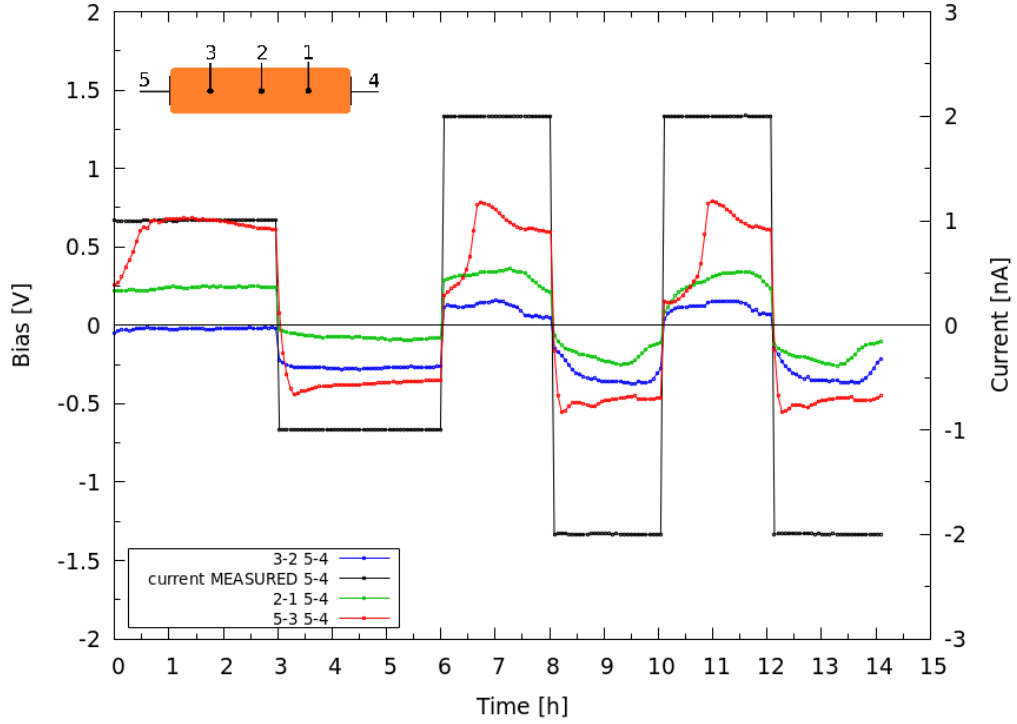
Figure 4.14: U-t-I evolution of sample CPB19, measured in group at 300K, chromium contacts.

Table 4.1: Calculated values at 300K for the region between contacts 5-3 and 3-2.

Interval No.	Drift velocity [cm/s]	El.field [V/cm]	Mobility [cm²/V.s]	Diffusion coeff. [cm²/s]
3	4.4e-4	4.1	1.1e-4	2.8e-6
4	2.6e-4	4.0	6.5e-5	1.7e-6
5	4.4e-4	4.0	1.1e-4	2.9e-6
6	2.2e-4	3.8	5.8e-5	1.5e-6

Table 4.2: Calculated values at 300K for the region between contacts 3-2 and 2-1.

Interval No.	Drift velocity [cm/s]	El.field [V/cm]	Mobility [cm²/V.s]	Diffusion coeff. [cm²/s]
3	1.3e-3	3.0	4.4e-4	1.1e-5
4	1.3e-3	3.3	4.0e-4	1.0e-5
5	6.6e-4	2.9	2.3e-4	5.9e-6
6	1.3e-3	3.2	4.1e-4	1.1e-5
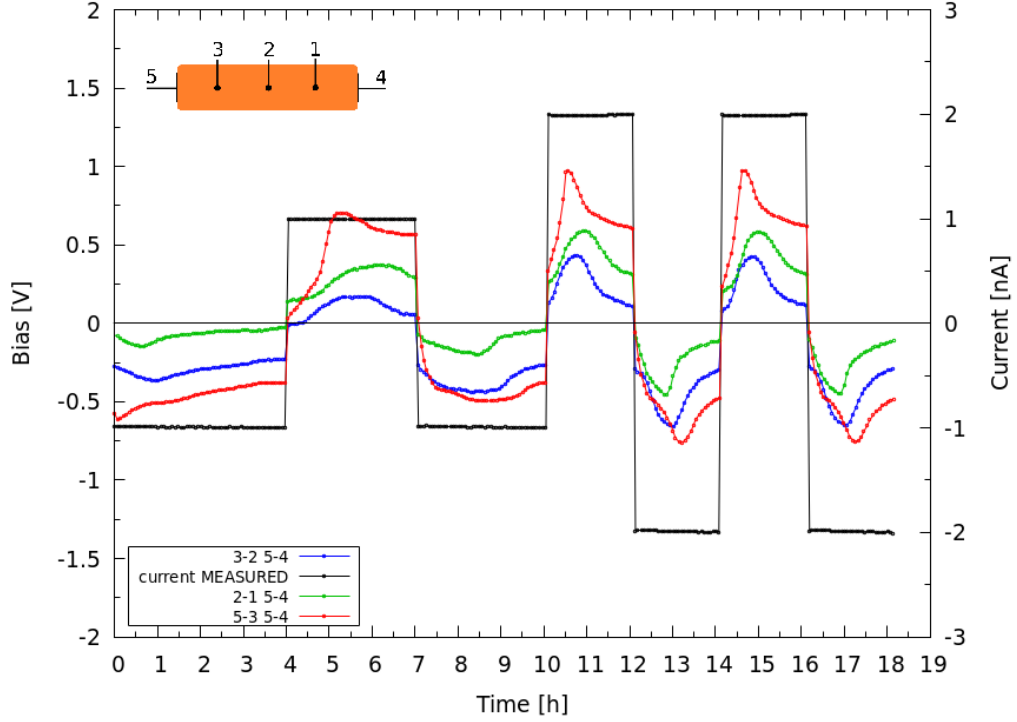
Figure 4.15: U-t-I evolution of sample CPB19, measured in group at 313K, chromium contacts.

Table 4.3: Calculated values at 313K for the region between contacts 5-3 and 3-2.

Interval No.	Drift velocity [cm/s]	El.field [V/cm]	Mobility [cm²/V.s]	Diffusion coeff. [cm²/s]
4	4.4e-4	2.2	2.0e-4	5.4e-6
5	4.4e-4	2.2	2.0e-4	5.3e-6
6	6.5e-4	2.2	3.0e-4	8.1e-6
7	4.4e-4	2.2	2.0e-4	5.4e-6

Table 4.4: Calculated values at 313K for the region between contacts 3-2 and 2-1.

Interval No.	Drift velocity [cm/s]	El.field [V/cm]	Mobility [cm²/V.s]	Diffusion coeff. [cm²/s]
4	4.3e-4	1.6	2.7e-4	7.2e-6
5	4.3e-4	1.8	2.4e-4	6.6e-6
6	6.6e-4	1.6	4.1e-4	1.1e-5
7	4.3e-4	1.7	2.5e-4	6.7e-6

Figure 4.16: U-t-I evolution of sample CPB19, measured in group at 333K, chromium contacts.

Table 4.5: Calculated values at 333K for the region between contacts 5-3 and 3-2.

Interval No.	Drift velocity [cm/s]	El.field [V/cm]	Mobility [cm²/V.s]	Diffusion coeff. [cm²/s]
3	3.3e-4	1.5	2.3e-4	6.5e-6
4	6.9e-5	1.5	4.8e-5	1.4e-6
5	3.3e-4	1.5	2.2e-4	6.4e-6
6	7.3e-5	1.4	5.1e-5	1.5e-6

Table 4.6: Calculated values at 333K for the region between contacts 3-2 and 2-1.

Interval No.	Drift velocity [cm/s]	El.field [V/cm]	Mobility [cm²/V.s]	Diffusion coeff. [cm²/s]
3	3.3e-4	0.8	3.9e-4	1.1e-5
4	4.3e-4	1.0	4.4e-4	1.3e-5
5	3.3e-4	0.8	4.1e-4	1.2e-5
6	4.3e-4	1.0	4.3e-4	1.2e-5

Conclusion

This thesis presents the results of measurements on the material CsPbBr3, which is a metal halide perovskite. It focuses on the characterization of this material, especially with chrome contacts, but also provides information on a sample with gold contacts. In the first chapter, it was explained why I want to deal with this material. Its advantages, differences and above all its potential in the field of applications were defined. In the following chapter, devoted to the theory, the issues of transport, $p - n$ transition and metal-semiconductor contact were discussed in detail. In the experimental part, I discussed the preparation of samples, contacting them, and went on to describe the measuring apparatus, including a detailed description of the most important properties of the devices used, taking into account our requirements and the nuances that affected our measurements. Everything was finished with a precise diagram of the complete measuring apparatus.

The chapter itself, dedicated to the presentation of the results and their discussion, is basically divided into three parts. The part dedicated to I-V characteristics was properly discussed. It only remains to add that a model was proposed that would explain the phenomenon that resistance increases at low voltages and currents, while resistance decreases at higher currents. However, further experiments will be necessary to confirm this model. In the following section, I deal with the issue of measurement depending on time. Among other things, the proven electromigration made it possible to determine the type of conductivity of the material. This is an important result, as attempts to determine this data using a more common method in a magnetic field were not successful due to the small signal-to-noise ratio. In the third part of this chapter, I focused on the calculation of transport quantities. By analyzing them, I came to believe that the detected non-monotonicity is related to the defect structure of the perovskite and also to the chemical reactions between the defects. However, a detailed analysis of such a model is beyond the scope of this thesis. Since the thesis is primarily experimental and the results will have to be verified in the future, the formulation of theoretical models is premature at this level.

Bibliography

[1] AKKERMAN, Quinten. *What Defines a Halide Perovskite?* ACS Energy Letters, 2020. ISSN 2380-8195. doi:10.1021/acsenergylett.0c00039

[2] XIAO, Zhengguo. *Giant switchable photovoltaic effect in organometal tri-halide perovskite devices.* Nature Materials 14(2), 2015. ISSN 1476-1122. doi:10.1038/nmat4150

[3] EAMES, C. *Ionic transport in hybrid lead iodide perovskite solar cells.* Nat Commun 6, 7497, 2015. doi:10.1038/ncomms8497

[4] ZHAO, Yicheng. *Correlations between Immobilizing Ions and Suppressing Hysteresis in Perovskite Solar Cells.* ACS Energy Letters 1(1), 2016. ISSN 2380-8195. doi:10.1021/acsenergylett.6b00060

[5] LIU, C. *Growth, characterization and photoelectrical properties of or-thorhombic and cubic CsPbBr3 single crystals.* J Mater Sci: Mater Electron 33, 24895–24905, 2022. doi:10.1007/s10854-022-09199-1

[6] GEORGE, Gibin. *Fundamentals of perovskite oxides: synthesis, structure, properties and applications.* Press Taylor and Francis Group, 2021. ISBN 978-0-367-35448-0.

[7] MIYASAKA, Tsutomu. *Perovskite Photovoltaics and Optoelectronics.* WILEY-VCH, 2022. ISBN 978-3-527-34748-3.

[8] SZE, S.M. *Physics of semiconductor devices.* 3rd ed. Hoboken, N.J.: Wiley-Interscience, 2007. ISBN 978-0-471-14323-9.

[9] FARRELL, Patricio. *Modelling charge transport in perovskite solar cells: Potential-based and limiting ion depletion.* Electrochimica Acta 390, 2021. doi:10.1016/j.electacta.2021.138696

[10] WANG, Li. *Ion migration in hybrid perovskites: Classifica-tion, identification, and manipulation.* Nano Today 44, 2022. doi:10.1016/j.nantod.2022.101503

[11] ALMORA, Osbel. *Coupling between Ion Drift and Kinetics of Electronic Current Transients in MAPbBr3 Single Crystals.* ACS Energy Lett., 7, 2022. doi:10.1021/acsenergylett.1c02578

[12] MOIA, Davide. *Ion Transport, Defect Chemistry, and the Device Physics of Hybrid Perovskite Solar Cells.* ACS Energy Lett., 6, 2021. doi:10.1021/acsenergylett.1c00227

[13] SENANAYAK, Satyaprasad. *Charge transport in mixed metal halide perovskite semiconductors.* Nature Materials, Volume 22, 2023. doi:10.1038/s41563-022-01448-2

[14] GARSIA-BELMONTE, Germà. *Effective Ion Mobility and Long-Term Dark Current of Metal Halide Perovskites with Different Crystallinities and Compositions.* Adv. Photonics Res., 3, 2200136, 2022. doi:10.1002/adpr.202200136

[15] KALTENBRUNNER, Martin. *Flexible high power-per-weight perovskite solar cells with chromium oxide–metal contacts for improved stability in air.* Nature Mater 14, 1032–1039, 2015. doi:10.1038/nmat4388

[16] HUANG, Wei. *Metal Halide Perovskite/Electrode Contacts in Charge-Transporting-Layer-Free Devices.* Adv. Sci.,9, 2203683, 2022. doi:10.1002/advs.202203683

[17] PAUPORTE, Tierry. *How do gold nanoparticles boost the performance of perovskite solar cells?.* Nano Energy 94, 106934, 2022. doi:10.1016/j.nanoen.2022.106934

[18] RAMAMURTHY, Praveen. *Role of electrodes on perovskite solar cells performance.* Journal of Micro and Smart Systems 11, 61–79, 2022. doi:10.1007/s41683-021-00089-y

[19] SUM, Tze-Chien. *Halide Perovskites - Photovoltaics, Light Emitting Devices, and Beyond.* Wiley-VCH Verlag GmbH, 2019. ISBN: 978-3-527-34111-5

[20] LI, Wei. *Hybrid Organic-Inorganic Perovskites.* Wiley-VCH Verlag GmbH, 2020. ISBN: 978-3-527-34431-4

[21] FUJIWARA, Hiroyuki. *Hybrid Perovskite Solar Cells.* Wiley-VCH Verlag GmbH, 2022. ISBN: 978-3-527-34729-2

[22] SEGAWA, Hiroshi. *Multifunctional Organic-Inorganic Halide Perovskite Applications in Solar Cells, Light-Emitting Diodes, and Resistive Memory.* Jenny Stanford Publishing Pte., 2022. ISBN: 978-981-4800-52-5

[23] AHMAD, Shahzada. *Perovskite Solar Cells Materials, Processes, and Devices.* WILEY-VCH GmbH, 2022. ISBN: 978-3-527-82578-3

[24] TILLEY, Richard. *Perovskites Structure–Property Relationships.* John Wiley and Sons, 2016. ISBN: 9781118935668

[25] LAALIOUI, Saida. *Perovskite-Based Solar Cells: From Fundamentals to Tandem Devices.* Walter de Gruyter GmbH, 2022. ISBN: 978-3-11-076061-3

[26] ARUL, Narayanasamy. *Revolution of Perovskite: Synthesis, Properties and Applications.* Springer Nature Singapore Pte, 2020. ISBN: 978-981-15-1267-4

[27] BISQUERT, Juan. *The Physics of Solar Energy Conversion.* Taylor and Francis Group, 2020. ISBN: 978-0-429-50587-4

[28] SHARMA, B.L.. *Metal-Semiconductor Schottky Barrier Junctions and Their Applications.* Plenum Press, 1984. ISBN: 978-1-4684-4655-5

[29] RHODERICK, E.H.. *Metal-Semiconductor Contacts.* 2nd ed. Oxford University Press, 1988. ISBN: 19859336

[30] COLINGE, Jean-Pierre. *Physics of Semiconductor Devices.* Kluwer Academic Publishers, 2005. ISBN: 978-0387285238

[31] ZHAO, Yicheng. *Discovery of temperature-induced stability reversal in perovskites using high-throughput robotic learning.* Nature Communications 2191, 2021. doi:10.1038/s41467-021-22472-x

List of Figures

List of Tables

List of Abbreviations

n_i .... Intrinsic carrier concentration
n_n .... Electron concentration in n-type semiconductor
p_p .... Hole concentration in p-type semiconductor
n_{no} .... n_n in thermal equilibrium
n_{po} .... p_p in thermal equilibrium
W_{Dn} .... Depletion width in n-type material
W_{Dp} .... Depletion width in p-type material
ρ .... Resistivity
ε_s .... Permittivity of semiconductor
N_D^+ .... Ionized donor impurity concentration
N_A^- .... Ionized acceptor impurity concentration
$\mathcal{E}_m$ .... Maximum electric field
ψ_n .... Potential at n-type boundary with respect to n-type bulk
ψ_p .... Potential at p-type boundary with respect to p-type bulk
E_i .... Intrinsic Fermi level
V .... Applied voltage
D .... Diffusion coefficient
D_n .... Diffusion coefficient for electrons
D_p .... Diffusion coefficient for holes
D_a .... Ambipolar diffusion coefficient
U .... Net recombination/generation rate
L_n .... Diffusion length of electrons
L_p .... Diffusion length of holes
J_0 .... Saturation current density
χ .... Electron affinity
ϕ_m .... Metal work function
D_{it} .... Interface-trap density
Q_{ss} .... Interface-trap charge density on the semiconductor
Q_{sc} .... Space charge density
Q_M .... Mobile-ionic-charge density
ε_i .... Permittivity of insulator
ε_0 .... Permittivity of vacuum
Ψ_s .... Surface potential with respect to bulk
N .... Density of states
W .... Thickness
F .... Fermi-Dirac distribution function
E_c .... Bottom edge of conduction band
v .... Carrier velocity
h .... Planck constant
Ψ_{bi} .... Built-in potential at equilibrium
A .... Effective Richardson constant for free electron
A^* .... Effective Richardson constant
m_0 .... Electron rest mass
m^* .... Effective mass
N_c .... Effective density of states in conduction band
v_D .... Effective diffusion velocity
F_c .... Fermi-Dirac distribution function for electrons
F_s .... Fermi-Dirac distribution function for semiconductor